# NorthWest Research Associates, Inc.

P.O. Box 3027 • Bellevue, WA 98009-3027

NWRA-CR-97-R169

18 July 1997

## Sea Ice Mechanics Research Progress

Report on Deliverables: Task 1 & Task 2

For Contract N00014-96-C-0096

Prepared by
Max D. Coon, Ph.D.

DTIC QUALITY INSPECTED 2

Prepared for

Office of Naval Research
Code ONR 322HL
Ballston Tower Centre One
800 Quincy Street
Arlington, VA 22217-5660

**19970724 100**

14508 N.E. 20th Street • Bellevue, WA 98007-3713 • (425) 644-9660 • FAX (425) 644-8422

NWRA-CR-97-R169                                    18 July 1997

# Sea Ice Mechanics Research Progress

Report on Deliverables: Task 1 & Task 2

For Contract N00014-96-C-0096

Prepared by
Max D. Coon, Ph.D.

Prepared for

Office of Naval Research
Code ONR 322HL
Ballston Tower Centre One
800 Quincy Street
Arlington, VA 22217-5660

# Sea Ice Mechanics Research Report

The deliverables for Contract N00014-96-C-0096 are published papers. Papers for Tasks 1 and 2 have been sent to the *Journal of Geophysical Research*, and copies are attached.

Task 1. The Architecture of an anisotropic elastic-plastic sea ice mechnics model

Task 2. Geophysical pack-ice stress measurements.

Task 1

**The Architecture of
An Anisotropic Elastic-Plastic Sea Ice Mechanics Model**

# The architecture of an anisotropic elastic-plastic sea ice mechanics model

Max D. Coon, Gerald S. Knoke, and Douglas C. Echert
NorthWest Research Associates, Inc.
Bellevue, WA, USA


Robert S. Pritchard
IceCasting, Inc.,
Seattle, WA, USA

## ABSTRACT

The architecture for a new large-scale (5 to 100 km, 1 hour to 1 day) sea ice dynamics model based on an anisotropic constitutive law is presented here. This architecture accounts directly for refrozen lead systems in the pack ice strength (with an anisotropic failure surface) and in the ice thickness distribution (with an oriented thickness distribution). The lower limit (5 km) of the model resolution is controlled by the fracture spacing of old, thicker ice and the maximum lead width. The upper limit of the model resolution (100 km) is controlled by curvature in the lead directions and variations in the lead width. These in turn are controlled by the variations in internal ice stress due to driving forces (winds and currents), which set the time resolution. This architecture features abrupt changes in the failure surface and the associated flow rule that cannot be averaged over a time step. In addition, the principal stress normal to a new lead must be zero as it opens.

This model has sub-scale simulations that allow for the inclusion of phenomena such as ridging, rafting, buckling, and fracture on the behavior of the ice. With this new ice constitutive law, it is possible to directly test the ice failure strength, plastic flow rule, and ice thickness distribution. The data most useful for this testing come from ice stress and position buoys together with SAR deformation data. Some data comparisons have already been made.

## INTRODUCTION

The ice model constitutive relations developed in this paper describe the anisotropic behavior of pack ice that is exhibited by the formation and evolution of leads in rafts and ridges. This model is intended for use when ice stress is important and has a marked influence upon the ice dynamics, which are the nine or ten months of the Arctic winter. During the summer, there is very little pack ice stress, the dynamics are little affected by the stress, and therefore there is no need for a constitutive law. The stress and deformation state of a two-dimensional element of pack ice is described by three stress components in the plane ($\sigma_{xx}$, $\sigma_{yy}$, $\sigma_{xy}$) (two normal and one shear) and three deformation rates (two normal and one shear).

In early ice dynamics models (Coon et al., 1974; Pritchard, 1975; Thorndike et al., 1975; Coon, 1980; Pritchard, 1981; Hibler, 1986), the behavior of the ice was taken to be isotropic. Therefore, the behavior was represented by two stress invariants and two deformation invariants. In these models, the ice is considered as a plastic material that has an elastic or viscous behavior for stresses below failure. The isotropic behavior is modeled by a yield function with fixed,

selected shape in the two stress-invariant space. The failure strength, i.e., size of the yield function, is controlled by one parameter, its compressive strength. Such a model can best describe pack ice when there are no active leads (no plastic deformation) or many (three or more) active lead directions in an element. Except near fixed boundaries, element sizes of hundreds of kilometers and time steps of weeks are required to have three or more active lead directions. Although many leads may show up in an aerial photo or satellite image, only a few are active.

Figure 1 in Stern et al. (1995), a typical ice motion product derived from SAR images, shows the relative ice motion during a three-day period in winter for an 80x300 km area. The relative ice motion is displayed as an array of vectors on a 5-km grid indicating the deviations from the mean ice displacement, or is displayed as the deformed configuration of an initially regular 5-km grid. There are clearly several regions of uniform motion separated by sharp discontinuities. Within the regions, most of the cells are rigid, with little or no deformation or area change. The discontinuities between the regions are essentially linear for the 100 kilometers seen in the figure. Therefore, isotropic models are not very good approximations of ice behavior on scales of 5 to 100 kilometers with time resolutions of fractions of a day to a few days. Much of the important physics is controlled, however, by leads, which need to be resolved on time scales that are fractions of a day.

Coon et al. (1992) suggested an anisotropic model to overcome these shortcomings of the isotropic model. In the present model, two types of ice behavior are considered. In the first behavior, the deformations occur as a combination of elastic stretching and plastic stretching of the one or two existing lead directions. In the second ice behavior, one or two leads are created and the deformations occur as a combination of elastic stretching and plastic stretching of the new and existing leads. This model determines the new lead directions. In both behaviors, the change of ice thickness distribution in the lead directions is calculated.

A large-scale ice-dynamics model can be described by considering a momentum balance, driving forces, and a constitutive law for the ice (see Coon et al., 1974). In the application considered for this model, resolutions of 5 to 100 km and 1 hour to 1 day are required. The time and space scales that can be resolved by this model are controlled by the driving forces and the constitutive equation. To accomplish this resolution, the pack ice is divided into two types, as illustrated in Figure 1:

- *Isotropic* ice is consolidated multi-year and heavy first-year ice with numerous flaws (brine-filled cracks) which limit its strength. *Isotropic* ice does not consist of single or multiple floes but of large clusters (1 to 20 km) of small, interlocking rigid fragments which are only 100 to 500 m in extent.
- *Oriented* 'ice' includes (following the nomenclature of WMO, 1970) open water, new ice, nilas, young ice, first-year ice, rafted ice, and ridged ice, when they occur in long, narrow features. First-year ice, rafted ice, and ridged ice are transferred to *isotropic* ice as soon as their strengths exceed that of isotropic ice. When not appearing in long, linear features, all these ice types are *isotropic* ice. In this paper, the term 'lead' is used broadly to describe these long, narrow features whether or not they contain open water, new ice, nilas, young ice, first-year ice, rafted ice, or ridged ice. There may or may not be an ice velocity discontinuity across the lead. Furthermore, parallel leads (lead systems) are not distinguished from a single lead in this model.

Table 1 lays out the architecture of this anisotropic elastic-plastic sea ice mechanics model. The three sections describe aspects of the model: ice dynamics model, *isotropic* ice behavior, and

*oriented* ice behavior. Each aspect includes a column of the type of data used to study each aspect, a list of the features of each aspect, and the sub-scale models needed to describe each aspect. The ice dynamics aspect is essentially similar to previous large-scale sea-ice-dynamics models. The *isotropic* ice behavior is substantially changed; deformations involve leads. The *oriented* ice behavior is new to pack-ice constitutive laws. Ice velocity solutions for the anisotropic problem are obtained in exactly the same way as they are for isotropic problems except that the constitutive law is different. The interpretation of the ice velocity field at each time step is now made in terms of leads to generate the new yield surface for the next time step. This procedure is very similar to changing the size of the yield surface in an isotropic model after each time step.

In the next section, the behavior of *isotropic* ice is examined, which leads into a discussion on the formation of new leads. A section on the behavior of *oriented* ice follows, including how the anisotropic yield surface is formed, the corresponding kinematics, and how the *oriented* ice thickness is redistributed due to deformations (which is the topic of a companion paper, Coon et al., 1997a).

## ISOTROPIC ICE

- *Isotropic* ice has an isotropic failure surface that remains relatively constant throughout the winter season. This failure surface can be written in terms of principal stresses.

*Isotropic* ice is the ice surrounding active lead systems; therefore, it may have a wide distribution of ice thickness and includes all multiyear ice and heavy first-year ice. Evans and Untersteiner (1971) showed how thermally induced ice stresses will cause bending failure and vertical cracks spaced at 100 to 300 meters, depending upon the ice thickness. As illustrated in Figure 2, *isotropic* ice is made up of large clusters of small, interlocking, closely fitting, angular, rigid fragments which are only 100 to 500 m in size because some of the thermal cracks flood and freeze. The cracks between the fragments are not flooded with sea water and offer a small amount of cohesion due to the material remaining below the crack. The small-scale mechanisms that form the *isotropic* ice and control its large-scale properties are thus crack formation, brine drainage into the cracks, and partial freezing of the brine if temperatures drop.

Since the *isotropic* ice consists of numerous fragments as shown in Figure 2, the new leads are never as straight as shown in Figure 1. As illustrated in Figure 2 by the bold lines, they will progress around the fragments following a general direction through the cells. Golombek and Banerdt (1990) discuss the allowable deviation of an acceptable crack direction from the preferred lead direction. A deviation of 15° from the preferred direction requires only a modest increase in stress at failure (less than 20% increase); the stress at failure is still a factor of ten less than that for a contiguous material.

### Description of *isotropic* ice strength

The *isotropic* ice is a homogeneous and plastic material with in-plane and out-of-plane failure mechanisms analogous to the Coulomb failure mechanisms in three-dimensional materials. The Coulomb failure mechanism is well characterized in the literature for soils (e.g., Bowles, 1968), for sea ice at the laboratory scale (e.g., Coon et al., 1984), and for pack ice (e.g., Pritchard, 1988). The Coulomb failure criterion states that the shear stress on any surface within

the material must not exceed the shear strength of that surface. The shear strength, in turn, depends linearly upon the normal stress on that surface.

We can evaluate the strength parameters for *isotropic* ice using sea-ice stress data such as that obtained during the U.S. Navy Office of Naval Research (ONR) Sea Ice Mechanics Initiative (SIMI) field program (see, for example, Coon et al., 1997b). Figure 3 shows SIMI stress data plotted as the shear-resultant invariant (half the difference of the principal stress-resultants) plotted against the pressure-resultant invariant (average of the principal stress-resultants). The data points in Figure 3 are the hourly averaged sea-ice stress measurements made by the authors during the SIMI program in 1993-94 in the Beaufort Sea, north of Alaska. We plotted the stress data in search of the envelope of the ice-stress data that corresponds to the failure surface of the pack ice. That is, pack-ice stress can have a wide range of values within the envelope, but, in a situation where it contacts the envelope, the pack ice fails. It forms a slip line or opens a lead system, thus limiting the stress.

The slopes and intercepts of the failure surface were chosen to enclose most of the stress data points. This failure surface is well represented by a Coulomb failure surface isotropic in three dimensions with an unconfined compressive strength of 250 kN/m and an unconfined tensile strength of 50 kN/m. The line representing the in-plane-shear failure is the middle line segment shown in Figure 3. The corresponding value for the friction angle is 42° and for the cohesion is 56 kN/m. These coefficients correspond to heavy pack ice with both first-year and multi-year ice. The unconfined compressive and tensile strengths, which are material constants, define this failure criterion. It is assumed that the cracks between the floe fragments control the strength of the *isotropic* ice.

To describe the stress state of pack ice, we introduce the stress-resultant as the product of the stress and the thickness of the ice. This is a plane-stress problem with $\sigma_1$ and $\sigma_2$ being the principal stress resultants in the plane of the ice, and the stress resultant normal to the ice, $\sigma_3$ , being zero. Failure occurs when the stress-resultant state is on the failure surface. Figure 4 shows an isotropic failure surface in principal stress-resultant coordinate system. The material properties that define this failure surface are the cohesion C and friction angle $\beta$. In-plane failure in the horizontal physical plane is represented by the two lines in the principal-stress coordinate system marked in Figure 4 as 1 and 2. The equations for these two failure surfaces are

$$\sigma_1(1 + \sin\beta) = \sigma_2(1 - \sin\beta) + 2C\cos\beta \tag{1}$$

$$\sigma_2(1 + \sin\beta) = \sigma_1(1 - \sin\beta) + 2C\cos\beta \tag{2}$$

In addition to these two failure surfaces, there are four other failure surfaces representing failures out of the plane of the ice sheet marked in Figure 4 as 3, 4, 5, and 6. These correspond to tensile failure (due to out-of-plane shear) and compressive failure (due to out-of-plane shear); the latter creates pressure ridges in thick ice. The equations for these four failure surfaces are

$$\sigma_1 = \sigma_t \tag{3}$$

$$\sigma_2 = \sigma_t \tag{4}$$

$$\sigma_1 = -\sigma_c \tag{5}$$

$$\sigma_2 = -\sigma_c \tag{6}$$

After comparing Figures 3 and 4, we can suggest other failure surfaces. The data in Figure 3 show an apparent maximum value for shear stress-resultant invariant of about 100 kN/m, corresponding to a Tresca or von Mises failure surface. This feature is shown in Figure 5a as an additional failure surface that is parallel to the pressure invariant axis; it corresponds to an in-plane, pure-shear failure that is independent of the normal stress-resultant and that generates no open water. The prior failure surfaces in Figure 5 are shown as tensile failure, in-plane shear failure, and compressive failures. Figure 5b shows an alternate with zero tensile strength; moving the tensile failure surfaces to the principal stress-resultant axes is a reasonable approximation of the stress data and will reduce difficulties anticipated in numerical solutions.

## FORMATION OF NEW LEADS

It is difficult to describe detailed physical mechanisms for the failure surfaces shown in Figures 3-5 and to determine corresponding flow rules. It is clear that new leads result from the failure of *isotropic* ice as well as the condition that open water can support no normal stress or shear stress. Therefore, a lead cannot form when there is compression in both principal directions. When one principal stress is zero, open water can be created in a lead parallel to the non-zero principal stress. The failure surface configuration shown in Figure 5b allows tensile failure to create open water in a lead parallel to the non-zero principal stress-resultant direction with a zero principal stress-resultant normal to the lead.

The failure surface in principal stress coordinates represents the failure of *isotropic* ice, but it does not address the yield surface or the flow rule. The stress state on a new lead must be examined to determine the yield surface. Figure 6 shows the lead coordinates as a set of $(\xi, \eta)$ axes rotated $\theta$ radians from the reference directions $(x, y)$. There is no traction across an open lead, so therefore the principal stresses are aligned with the lead and the principal stress normal to the lead is zero. For example, if we have $\sigma_1 = 0$, then the stresses are known to be

$$\sigma_{\xi\xi} = \sigma_2 \qquad \sigma_{\eta\eta} = 0 \qquad \sigma_{\xi\eta} = 0 \tag{7}$$

The stress and deformation of a lead at its creation are reported by Coon et al. (1995a). Simultaneous measurements of sea ice stress on both sides of a lead, ice motion from sequential SAR imagery, and ice motion from drifting GPS/Argos buoys are compared. The lead, which appeared early in Day 35 (Feb. 4), 1994, was observed, relative motions were calculated across and along the lead direction, and stresses were transformed to this same coordinate system. The lead orientation and approximate location were determined from SAR images of the pack ice surrounding the SIMI camp, as well as net ice motion at 3-day intervals. The ice motion around the lead was provided in greater temporal detail by an array of drifting GPS/Argos buoys producing hourly positions. Sea ice stress was measured on each side of the lead using flat-jack sensors; Figure 7 shows the stress components in lead coordinates.

Shortly before the lead-opening motion is apparent in the ice motion data, the ice-stress state abruptly changes from bi-axial compression to uni-axial compression with traction on the lead near zero. The stress path in stress-resultant-invariant space is shown in Figure 8. After the lead is opened, the principal directions of strain rate and stress no longer coincide (Figure 9). Therefore, pack ice with an active lead is a highly anisotropic material; isotropic models cannot

describe this behavior since they assume that the principal directions of stress and stretching always coincide.

In stress space, the yield is occurring on the $\sigma_2$ axis. As long as there is open water in the new lead, the stress state must be represented by Equation (7), and, therefore, the lead opening and shearing motions represent deformations on a new yield surface defined by Equation (7). This yield surface is anisotropic and, in $\sigma_{xx}$-$\sigma_{yy}$-$\sigma_{xy}$ space, the equations for the stress are a parametric representation of a line in stress space in terms of $\sigma_{\xi\xi}$:

$$\sigma_{xx} = \frac{\sigma_{\xi\xi}}{2}(1 - \cos2\theta)$$

$$\sigma_{yy} = \frac{\sigma_{\xi\xi}}{2}(1 + \cos2\theta)$$

$$\sigma_{xy} = -\frac{\sigma_{\xi\xi}}{2}(\sin2\theta)$$

(8)

For any lead orientation, Equation (8) is a family of lines that pass through the origin of stress space, forming the tensile cutoff cone shown in Figure 5b.

## ORIENTED ICE

- *Oriented* 'ice' provides orientation to the strength of the pack ice. Each lead has its own orientation.

The *oriented* ice in leads and refrozen leads causes anisotropy in the strength of the pack. The constituents of *oriented* ice include (following the nomenclature of WMO, [1970]) open water, new ice, nilas, young ice, first-year ice, rafted ice, and ridged ice when they occur in long, narrow features.

### Yield surface for *oriented* ice and flow rule

The generic shape of the lead yield surface is shown in Figure 10a as a rectangular prism with rounded ends. The prism represents the failure and yield surface for the *oriented* ice in one lead. The stress parallel to the lead ($\sigma_{\xi\xi}$) is aligned with the long-axis of the prism, $\sigma_{nn}$ is the stress normal to the lead, and $\sigma_{\xi n}$ is the shear stress on the lead. When one lead direction is active, the anisotropic yield surface for the pack ice consists of the prism and the rounded ends that are contributed by the failure surface for the *isotropic* ice. When the stress state lies on one of these ends, the *isotropic* ice will fail. When the stress state lies on the sides of the prism, the lead fails by a combination of shearing and opening or closing. The top and bottom surfaces in Figure 10a correspond to shear yield of the oriented ice in the lead; the left surface corresponds to compressive failure (rafting and ridging); and the right surface corresponds to tensile failure (opening).

In this stress space, the *oriented* ice yield surface is a prism of constant cross-section that lies at 45° to the pressure invariant axis. The pressure invariant axis is shown bisecting the angle between the parallel stress ($\sigma_{\xi\xi}$) and the normal stress ($\sigma_{nn}$). As an example, the yield surface for a lead with open water is a line lying along the $\sigma_{\xi\xi}$-axis, as shown in Figure 10b. As ice grows in the lead, the cross-section of the yield surface grows as well. Practically speaking, the precise shape of that cross-section is less important than its overall dimensions because the dimensions

change rapidly due to ice growth and deformation. Suitable cross-sections include a rectangle, a diamond, and an ellipse, as illustrated in Figure 10c. Future work may determine whether it is a rectangle, diamond, oval, ellipse, or other shape, but each yield surface will have a maximum stress perpendicular to the lead (tensile strength), a minimum stress perpendicular to the lead (compressive strength), and a maximum shear stress magnitude (shear strength), associated with a specific lead direction. A discussion of the yield strength of *oriented* ice is now a matter of defining these strength parameters.

It is difficult to visualize the intersection of the lead yield surface and the isotropic failure surface. Figure 10d shows the $\sigma_{\xi\eta} = 0$ slice of the isotropic failure surface from Figure 4 in the same lead-stress coordinates used in Figure 10a. The slice of the lead's rectangular prism is shown as two lines parallel to the $\sigma_{\xi\xi}$-axis. When $\sigma_{\xi\eta} = 0$, the other two lead-stress coordinates ($\sigma_{\xi\xi}$ and $\sigma_{\eta\eta}$) are the principal stresses and the isotropic failure surface lies in the ($\sigma_{\xi\xi}$-$\sigma_{\eta\eta}$) plane.

When there are two oriented yield surfaces, then the isotropic failure surface may not come into play at all. For example, if there two leads with open water that are not parallel, then each contributes a line yield surface and their intersection at the origin is the yield surface, implying a null stress state and free drift of the pack ice. A lead with open water combined with a lead with thin ice will generate a yield surface consisting of a line chopped off by the rectangular prism of the other lead. As ice grows in both leads, both yield surfaces grow in size. The rectangular prism grows beyond the isotropic failure surface, and the line grows to a rectangular prism. Perhaps much of the time, the ridging strengths of several old leads limit the compressive strength of the pack ice, not the isotropic compressive strength discussed in Section 2.

## Failure mechanisms of *oriented* ice

Consider the rectangular lead yield surface in Figure 10c. As shown in Figure 11, each side of the rectangle represents a lead-ice failure mechanism: opening, closing, the opposite side of the lead moving to the right (positive shear), or the opposite side moving to the left (negative shear). The dimensions of the rectangle depend only on the thickness of the thinnest ice within the refrozen lead system. When the stress resultant touches this rectangle, plastic flow occurs within the lead system; i.e., the lead ice opens, closes, or shears. A tensile strength, $\sigma_t$, a compressive strength, $\sigma_c$, and a shear strength, $\sigma_s$, define the four sides of the rectangle. As a consequence of the normal flow rule, the side of the rectangle with positive shear stress (the top side as shown) represents stress states with plastic flow of the lead ice in pure positive shear (no opening or closing of the lead) since the outward normal is in the direction of positive shear stress. The right side is pure opening, the bottom is pure negative shear, and the left is pure compression. At the top right corner, a range of stretching corresponds to the fan of outward normals between positive shear and opening. The other corners have similar fans of outward normals. Thus, this rectangular yield surface allows all plastic stretching vectors in this plane. In 3-D stress space, the four sides of the rectangle represent planar faces that extend indefinitely in the stress resultant direction parallel to the lead. The component of stretching parallel to the lead is zero and corresponds to a component out of the plane shown in Figure 11. If necessary, such ice deformations are accomplished by deforming another existing lead system or by contacting the failure surface for the *isotropic* ice and creating another one or two lead systems.

## Form of yield function in x-y-z stress coordinates

The four plastic yield functions that define the four sides of the rectangular prism are given by the following equations:

$$\phi_{jt} = \sigma_I - \sigma'_{xx}\cos2\theta_j - \sigma_{xy}\sin2\theta_j - \sigma_{jt}$$
$$\phi_{jc} = -\sigma_I + \sigma'_{xx}\cos2\theta_j + \sigma_{xy}\sin2\theta_j - \sigma_{jc}$$
$$\phi_{jp} = -\sigma'_{xx}\sin2\theta_j + \sigma_{xy}\cos2\theta_j - \sigma_{js}$$
$$\phi_{jn} = \sigma'_{xx}\sin2\theta_j - \sigma_{xy}\cos2\theta_j - \sigma_{js}$$

(10)

where $\theta_j$ is the angle from x-axis to the direction parallel to the j-th lead and where the subscripts t, c, p, and n refer to the tension, compression, positive shear, and negative shear sides of the rectangle, respectively. These four sides form a rectangular prism that always lies at a 45° angle to the $\sigma_I$-axis (the axis of the cone for the *isotropic* ice failure surface). The lead angle $\theta_j$ defines the orientation of the j-th prism around the $\sigma_I$-axis. In stress-resultant space, $2\theta_j$ is the angle between the $\sigma_I$-$\sigma'_{xx}$ plane and the plane containing the $\sigma_I$-axis and the j-th yield surface prism.

## Kinematic equations for pack ice with deformations along leads

Coon et al. (1997a) described the kinematics and ice-thickness redistribution of pack ice while accounting for lead and ridge orientation. The pack ice deformations are described in terms of velocity discontinuities rather than invariants, allowing direct interpretation of open-water production and ridging. The behavior requires an oriented ice-thickness distribution to account for the growth and ridging of ice in refrozen leads.

Each active lead direction contributes to the plastic deformation of the pack ice. The pack ice motion is therefore the sum of the contributions of lead directions. It is assumed that there are negligible deformations of the isotropic ice between the leads (e.g., elastic deformations). In this model, the velocity derivative normal to the lead directions is the only part of the kinematics that affects ice-thickness redistribution in the leads.

## Ice-thickness redistribution

The distribution of ice thickness at each lead orientation can be described much as others have described the distribution of ice thickness (e.g., Thorndike et al., 1975). Coon et al. (1997a) characterized these ice-thickness distributions assuming isotropic ice has one ice-thickness category and oriented ice has four ice-thickness categories in N lead systems, and developed the mathematical equations and calculation procedures for the ice-thickness redistribution. These results could be adapted to any number of ice thickness categories.

Once the ice thickness distribution in a lead system is updated, the strength parameters for that lead can calculated based on the thickness of the thinnest ice thickness category available. The tensile strength is near zero. The compressive strength can be estimated from theories, numerical models (Hopkins, 1994), laboratory data, and field data for buckling (Coon et al., 1989a), rafting (Pritchard et al., 1995), and ridging (Parmerter and Coon, 1972) of lead ice. The shear strength can be estimated from buckling and the shear strength of rubble ice (Weiss et al., 1981; Coon et al., 1995b). All vary with the ice thickness. Given these strengths, the yield surface associated with each lead is combined with the *isotropic* ice failure surface into a single

failure surface. It is of interest to note that the *oriented* ice yield surfaces will change quickly over hours or days while the isotropic failure surface may be essentially constant for a whole season.

## SUMMARY AND CONCLUSIONS

The anisotropic sea-ice model describes the behavior of individual lead systems within a general framework of plasticity. The yield surface and normal flow rule of each lead system is viewed in coordinates aligned with it. This view is two dimensional because only the traction across the lead affects its behavior until surrounding isotropic ice fails. When a lead first opens, its yield surface is a line in stress space; that is, it cannot sustain normal or shear stress across it. Its thickness distribution evolves thermally. When thicker ice is located in the lead, its compressive and shear strengths are larger. These strengths can be estimated from selected processes such as buckling, shearing, rafting, or ridging.

The failure surface of the surrounding isotropic ice is a body of revolution in stress space, or a polygon in stress invariant space, as in isotropic models. It is bounded by tensile cutoff (a principal stress is zero), a maximum shear strength, and a cap on the compressive end.

A new lead may form when at least one principal stress is zero. Orientation of the new lead is determined by the orientation of principal direction of the stress tensor at this time. There is no requirement that principal directions of stress and stretching be aligned. As the lead subsequently deforms, the direction of principal stretching is limited by the restriction that stretching along the lead direction is zero. This condition, however, does not cause the direction of principal stretching to be aligned with the lead. Once the refrozen lead ice has significant compressive and shear strength, the principal direction of stress can be arbitrary. Leads therefore allow and promote anisotropic behavior in pack ice.

We have assumed that the isotropic ice is fractured in all directions and has zero tensile strength in all directions. If the sea ice is sheared under compressive stresses, it deforms along velocity discontinuity lines (closed and shearing leads). Under these conditions, the shear stress invariant is at its maximum value (analogous to Tresca and von Mises failure criteria), two orthogonal (closed and shearing) lead directions exist, and they bisect the principal directions. Such deformations do not cause further damage to the isotropic material, and future lead formation is not affected by these deformations.

This anisotropic model provides an opportunity to describe the formation of open water more accurately, even to the extent of defining its orientation, which can be compared directly with new leads observed in SAR imagery. Although the anisotropic constitutive law was developed to describe behavior on smaller scales, say 5 km resolution, by incorporating the physical behavior from even smaller scales, it also improves on our ability to describe the one variable that is most critical to climate dynamics modeling, the amount of open water.

## NOTATION

| | |
|---|---|
| $C$ | cohesion (a stress resultant) in pack ice (N/m) |
| $x, y$ | reference coordinate system (m) |
| | |
| $\beta$ | friction angle in pack ice (radians) |
| $\theta, \theta_j$ | in physical space, angle from x-axis to (j-th) lead direction (radians) |
| $\xi, \eta$ | lead coordinate system (m) |

| | |
|---|---|
| $\sigma_1, \sigma_2$ | principal stress resultants (N/m) |
| $\sigma_I, \sigma_{II}$ | first and second stress invariant resultants (pressure and shear invariant resultant, respectively) (N/m) |
| $\sigma_{xx}, \sigma_{yy}, \sigma_{xy}$ | components of stress resultant tensor in x-y coordinates (N/m) |
| $\sigma'_{xx}$ | xx-deviatoric stress resultant in x-y coordinates (N/m) |
| $\sigma_{\xi\xi}, \sigma_{\eta\eta}, \sigma_{\xi\eta}$ | components of stress resultant tensor in lead coordinates (N/m) |
| $\sigma_c, \sigma_t$ | unconfined compressive and tensile strength resultants of the isotropic ice, respectively (N/m) |
| $\sigma_{cj}, \sigma_{sj}, \sigma_{tj}$ | compressive, shear, and tensile strength resultant of j-th lead system, respectively (N/m) |
| $\phi_j$ | plastic yield function for j-th lead direction (N/m) |
| $\phi_{jt}, \phi_{jc}, \phi_{jp}, \phi_{jn}$ | plastic yield functions for tension, compression, positive shear, and negative shear for j-th lead direction (N/m) |

## Acknowledgments

## REFERENCES

Bowles, J. E., *Foundation Analysis and Design*, McGraw-Hill Book Company, New York, NY, 1968.

Coon, M. D., G. A. Maykut, R. S. Pritchard, D. A. Rothrock, and A. S. Thorndike, Modeling the pack ice as an elastic-plastic material, in *AIDJEX Bulletin*, No. 24, pp. 1-106, University of Washington, Seattle, 1974.

Coon, M. D., A review of AIDJEX modeling, in *Sea Ice Processes and Models*, edited by R. S. Pritchard, pp. 12-27, University of Washington Press, Seattle, 1980.

Coon, M. D., R. J. Evans, and D. H. Gibson, Failure criteria for sea ice and loads resulting from crushing, in *Proceedings of International Association for Hydraulic Research Ice Symposium 1984*, Vol. III, Hamburg, 1984.

Coon, M. D., G. S. Knoke, and P. A. Lau, Time dependent effects on ridge initiation in sea ice leads, in *Proceedings of the OCEANS'89 Conference*, Seattle, WA, September, 1989a.

Coon, M. D., P. A. Lau, S. H. Bailey, and B. J. Taylor, Observations of Ice Floe Stress in the Eastern Arctic, *POAC '89, The 10th International Conference on Port and Ocean Engineering under Arctic Conditions*, Volume 1, Proceedings, Luleå, Sweden, 1989b.

Coon, M. D., D. C. Echert, and G. S. Knoke, Pack ice anisotropic constitutive model, in *IAHR 92, Proceedings of the 11th International Symposium on Ice*, p. 1188, Banff, Alberta, 1992.

Coon, M. D., D. C. Echert, G. S. Knoke, J. E. Overland, S. Salo, R. S. Pritchard, D. A. Rothrock, and H. L. Stern, Sea Ice Deformation and Stress, a Comparison across Space Scales, in *Proceedings of the Sea Ice Mechanics and Arctic Modeling Workshop*, Anchorage, AK, April 25-28, Vol. 2, 1995a.

Coon, M. D., D. C. Echert, and G. S. Knoke, Force-Displacement Measurements of a First-Year Pressure Ridge Keel, in *AMD-Vol. 207, Ice Mechanics - 1995*, American Society of Mechanical Engineers, pp. 239-254, 1995b.

Coon, M. D., G. S. Knoke, D. C. Echert, and R. S. Pritchard, An oriented thickness distribution for sea ice, to be submitted to JGR in April, 1997a.

Coon, M. D., G. S. Knoke, and D. C. Echert, Geophysical pack-ice stress measurements, to be submitted to JGR in April, 1997b.

Evans, R. J., and N. Untersteiner, Thermal cracks in floating sea ice sheets, *Journal of Geophysical Research*, Vol. 76(3), pp. 694-703, 1971.

Golombek, M. P. and W. B. Banerdt, Constraints on the Subsurface Structure of Europa, *Icarus*, Vol. 83, pp. 441-452, 1990.

Hibler, W. D. III, Ice dynamics, in *The Geophysics of Sea Ice*, H. Untersteiner, editor, pp. 577-640, Plenum Press, New York, 1986.

Hopkins, M. A., On the Ridging of Intact Lead Ice, *Journal of Geophysical Research*, Vol. 99, No. C8, pp. 16,351-16,360, 1994.

Lau, P. A. and G. S. Knoke (1991) "Arctic Ice Stress Measurements," OCEANS'91 Proceedings, Ocean Technologies and Opportunities in the Pacific for the 90's, Volume 1, pp. 645-650.

Parmerter, R. R. and M. D. Coon, A Model of Pressure Ridge Formation in Sea Ice, *Journal Geophysics Research*, Vol. 77, pp. 6565-6575, 1972.

Pritchard, R. S., An elastic-plastic constitutive law for sea ice, *Journal of Applied Mechanics*, Vol. 42, No. 2, pp. 379-384, June, 1975.

Pritchard, R. S., Mechanical behavior of pack ice, in *Mechanics of Structured Media*, Part A, edited by A. P. S. Selvadurai, Elsevier, New York, pp. 371-405, 1981.

Pritchard, R. S., Mathematical characteristics of sea ice dynamics models, *Journal of Geophysical Research*, Vol. 93, No. C12, pp. 15,609-618, 1988.

Pritchard, R. S., M. D. Coon, D. C. Echert, and G. S. Knoke, Ice block override, Abstract and presentation at the AGU 1995 Fall Meeting, San Francisco, CA, December, 1995.

Stern, H. L., D. A. Rothrock, and R. Kwok, Open water production in Arctic sea ice: Satellite measurements and model parameterizations, *Journal of Geophysical Research*, Vol. 100, No. C10, pp. 20,601-20,612, October 15, 1995.

Thorndike, A. S., D. A. Rothrock, G. A. Maykut, and R. Colony, The Thickness Distribution of Sea Ice, *Journal of Geophysical Research*, Vol. 80, No. 33, November 20, pp. 4501-4513, 1975.

Weiss, R. T., A. Prodanovic, and K. N. Wood, Determination of ice rubble shear properties, in *Proceedings of IAHR International Symposium on Ice, Quebec*, Volume II, pp. 860-870, 1981.

World Meteorological Organization, WMO sea-ice nomenclature, Geneva, Switzerland, WMO/OMM/BMO-No. 259, TP. 145, 147 pp., 1970.

**Table 1.** Architecture of Anisotropic Model

| Data | Large-scale sea ice dynamics model | Sub-scale models |
|---|---|---|
| Air pressure<br>Air drag coefficient<br>Ocean currents<br>Ocean drag coefficients<br>Air temperature<br>Ice thickness distribution | Momentum balance<br>Driving forces: air stress, water stress<br>Resulting forces: Coriolis forces, ice stress<br>Resulting kinematics: Ice velocity, ice deformation, ice thickness redistribution<br><br>Ice stress and deformation are related through the Constitutive Law<br><br>Pack Ice Constitutive Law<br>• For space scale 5 - 100 km and time scale 1 hr - 1 day<br>• Elasto-plastic or visco-plastic formulation<br>• Combines *isotropic* ice (multiyear and heavy first-year) and *oriented* ice (1 or 2 lead directions provide orientation). | Atmospheric boundary layer<br>Ocean boundary layer<br>Ocean currents |
| Data | *Isotropic* ice behavior | Sub-scale models |
| Stress<br>Acoustic<br>Fracture<br>Temperature | *Isotropic* Ice:<br>MY and heavy FY<br><br>*Isotropic* ice behavior:<br>Active cracks from thermal causes ~300 meter fragments.<br>In-plane and out-of-plane shear failure mechanisms<br>Lead orientation | Thermal stress<br>Bending fracture<br>Crack production |
| Data | *Oriented* ice behavior | Sub-scale models |
| Stress<br>Ridge profiles<br>Ice friction<br>Lead deformation<br>Brine rejection | *Oriented* ice:<br>*Isotropic* ice with 1 or 2 lead directions<br><br>*Oriented* ice behavior:<br>Ice growth in leads<br>Yield surface for leads and ridges<br>Ice redistribution | Ice buckling, rafting, ridging<br>Noise generation |
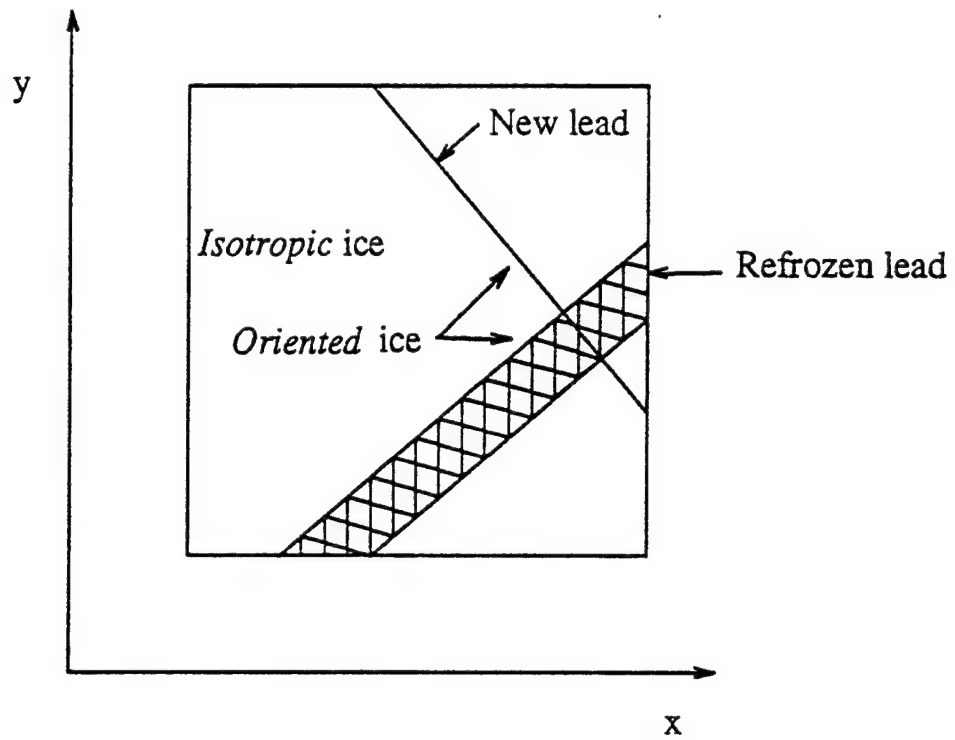
**Figure 1.** Region of pack ice with a wide refrozen lead and a narrow new lead forming in the *isotropic* ice.
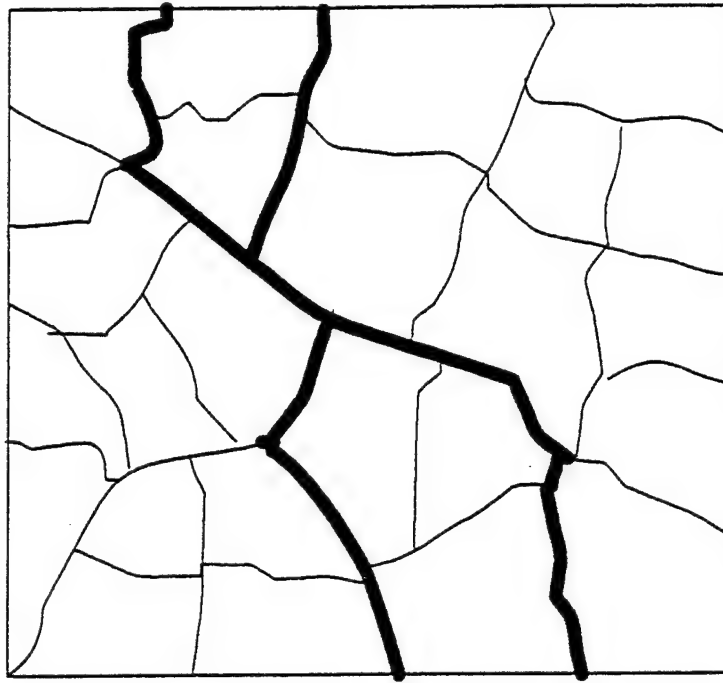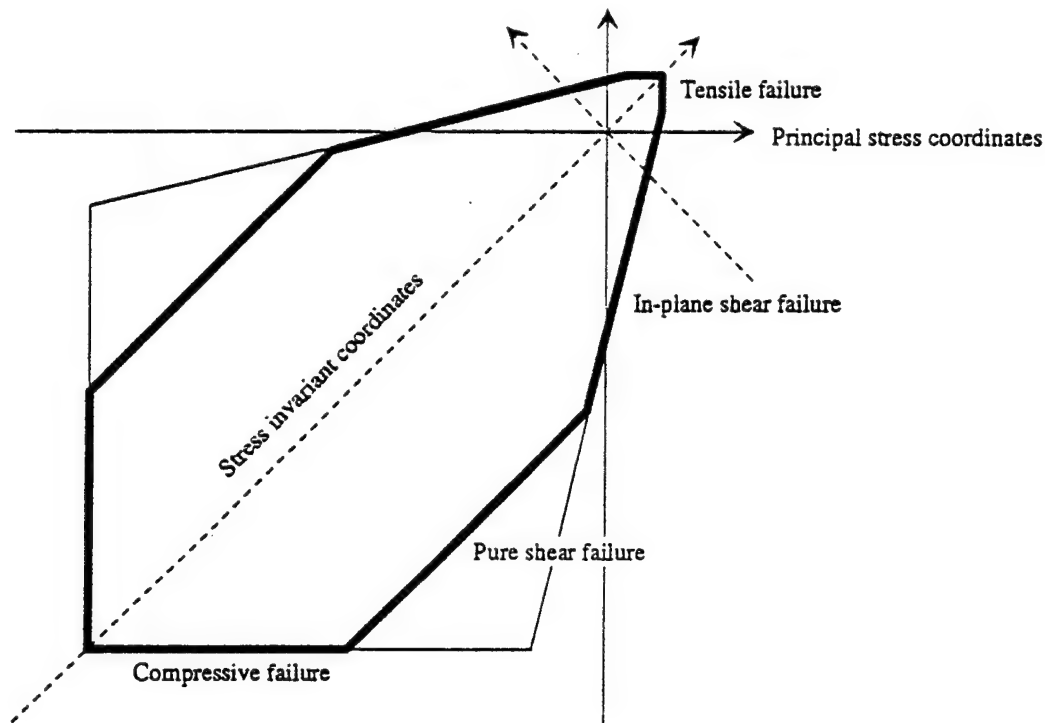
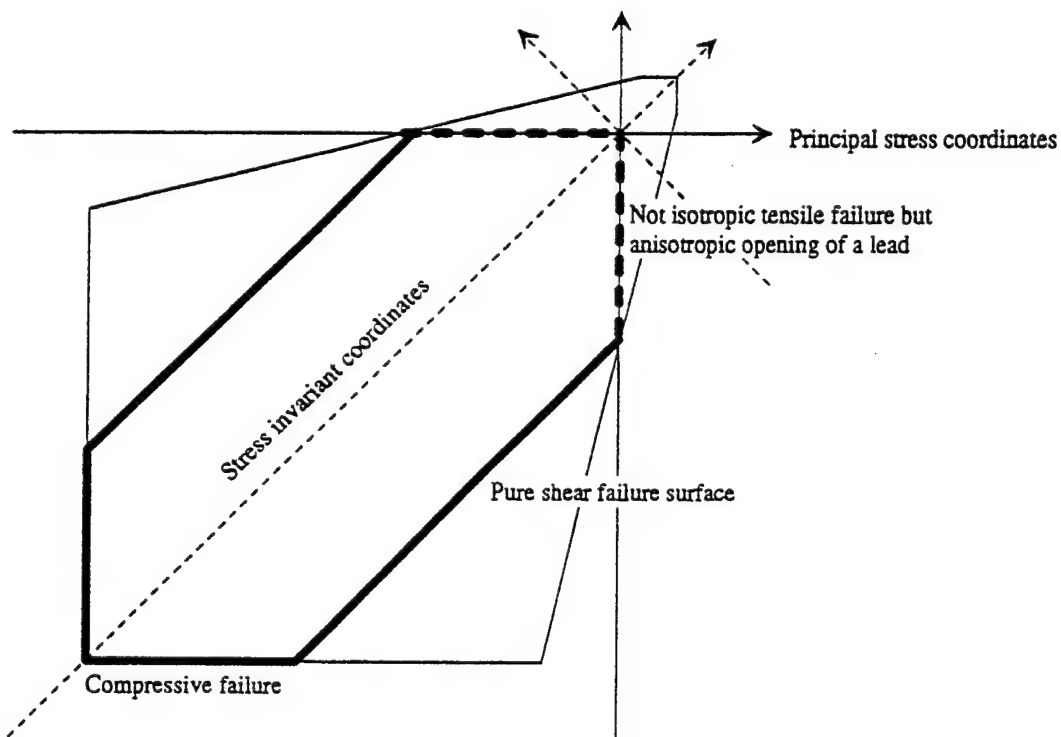**Figure 2.** Possible leads resulting from failure of fragmented *isotropic* ice
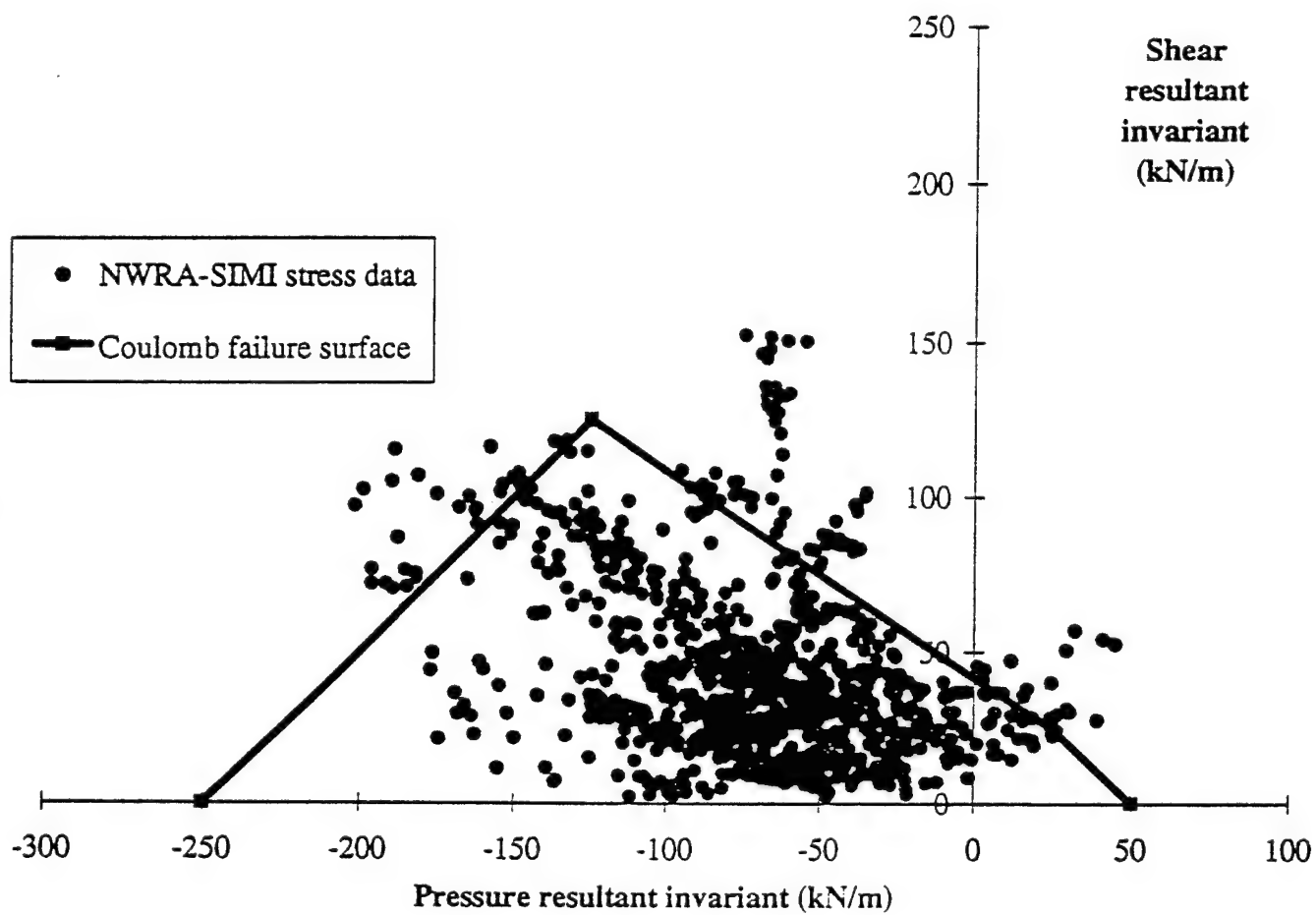
**Figure 3.** Coulomb failure surface determined from upper bound of measured ice stress-resultant (from Coon et al., 1997b)
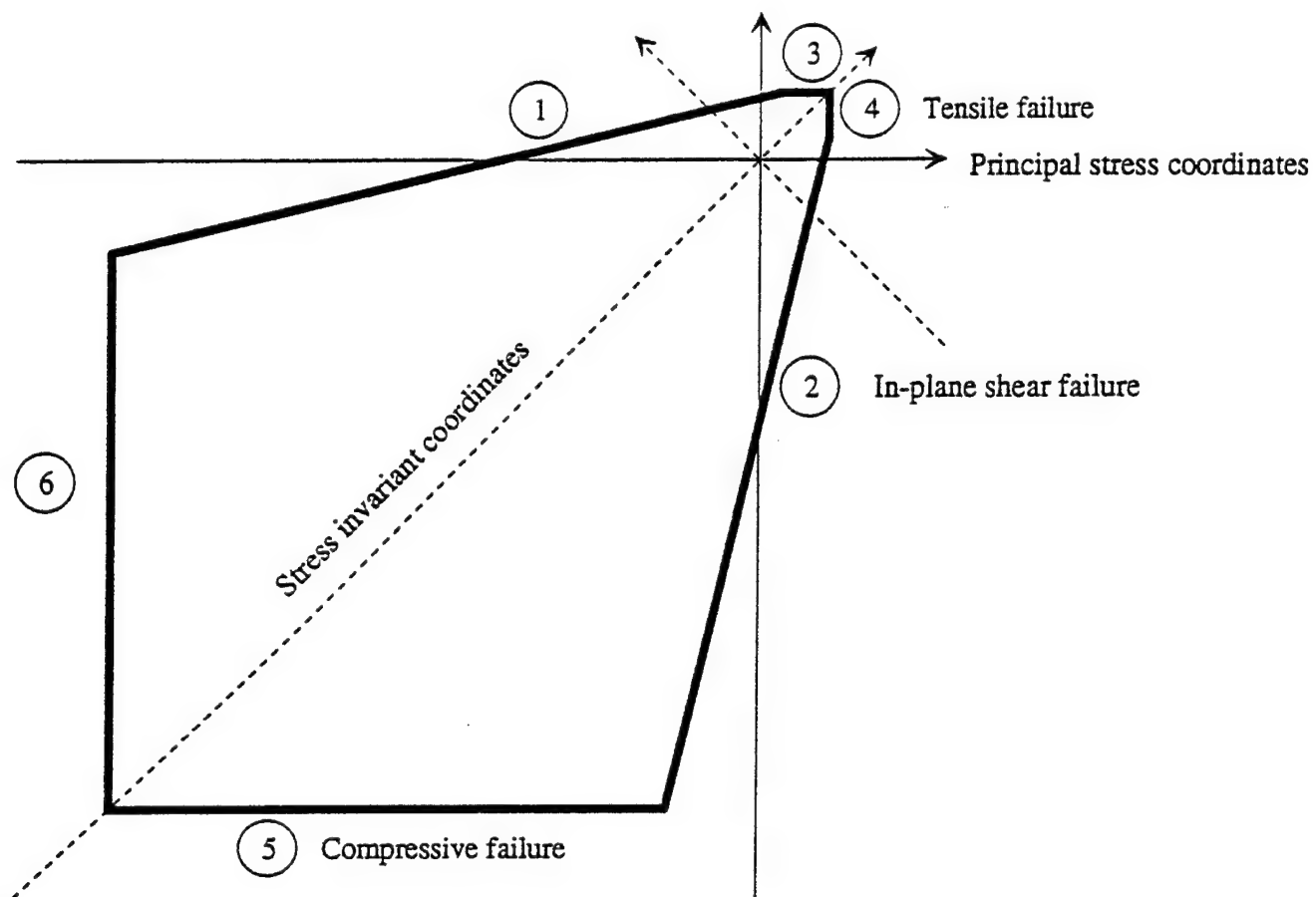
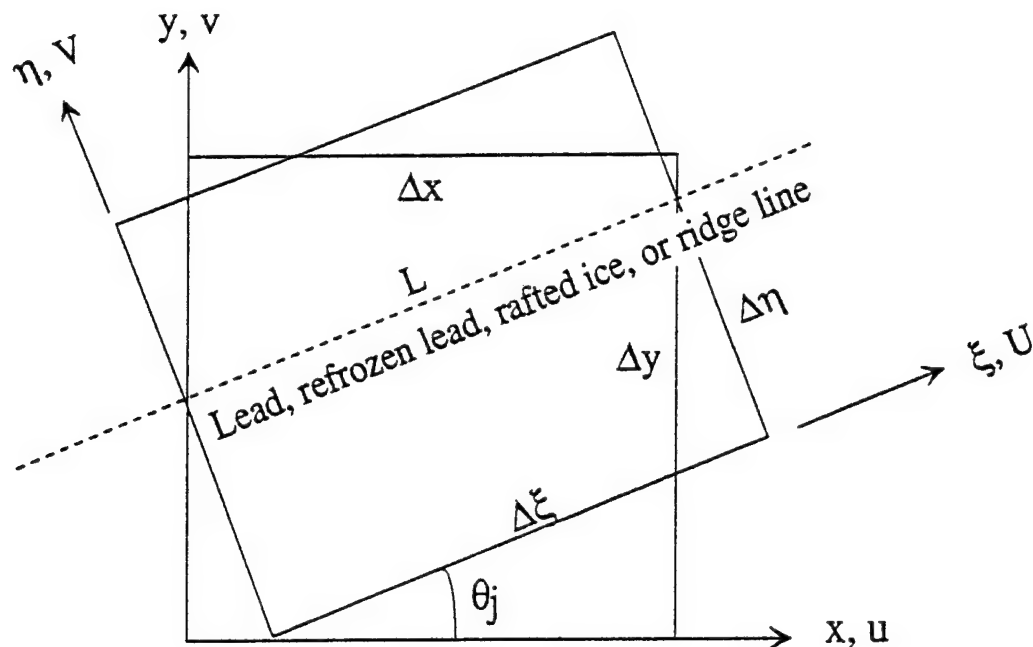**Figure 4.** Isotropic failure surface with tensile and compressive end caps

(a) With isotropic pure-shear failure surface added.



(b) With tensile strength reduced to zero and isotropic pure-shear failure surface added to Figure 4.

**Figure 5.** Alternate isotropic failure surfaces for pack ice

| | |
|---|---|
| x, y | Reference coordinate system (m) |
| u, v | Velocity components in reference coordinate system (m/s) |
| $\Delta x, \Delta y$ | Cell dimensions in reference coordinate system (m) |
| $\theta_j$ | Angle from x-axis to j-th lead direction (radians) |
| $\xi, \eta$ | Lead coordinate system (m) |
| U, V | Velocity components in lead coordinate system (m/s) |
| $\Delta\xi, \Delta\eta$ | Cell dimensions in lead coordinate system (m) |
| $\Delta U, \Delta V$ | Velocity jumps across $\Delta\eta$ in lead coordinate system (m/s) |

**Figure 6.** Coordinate system and velocity components of a rotated cell aligned with the lead.
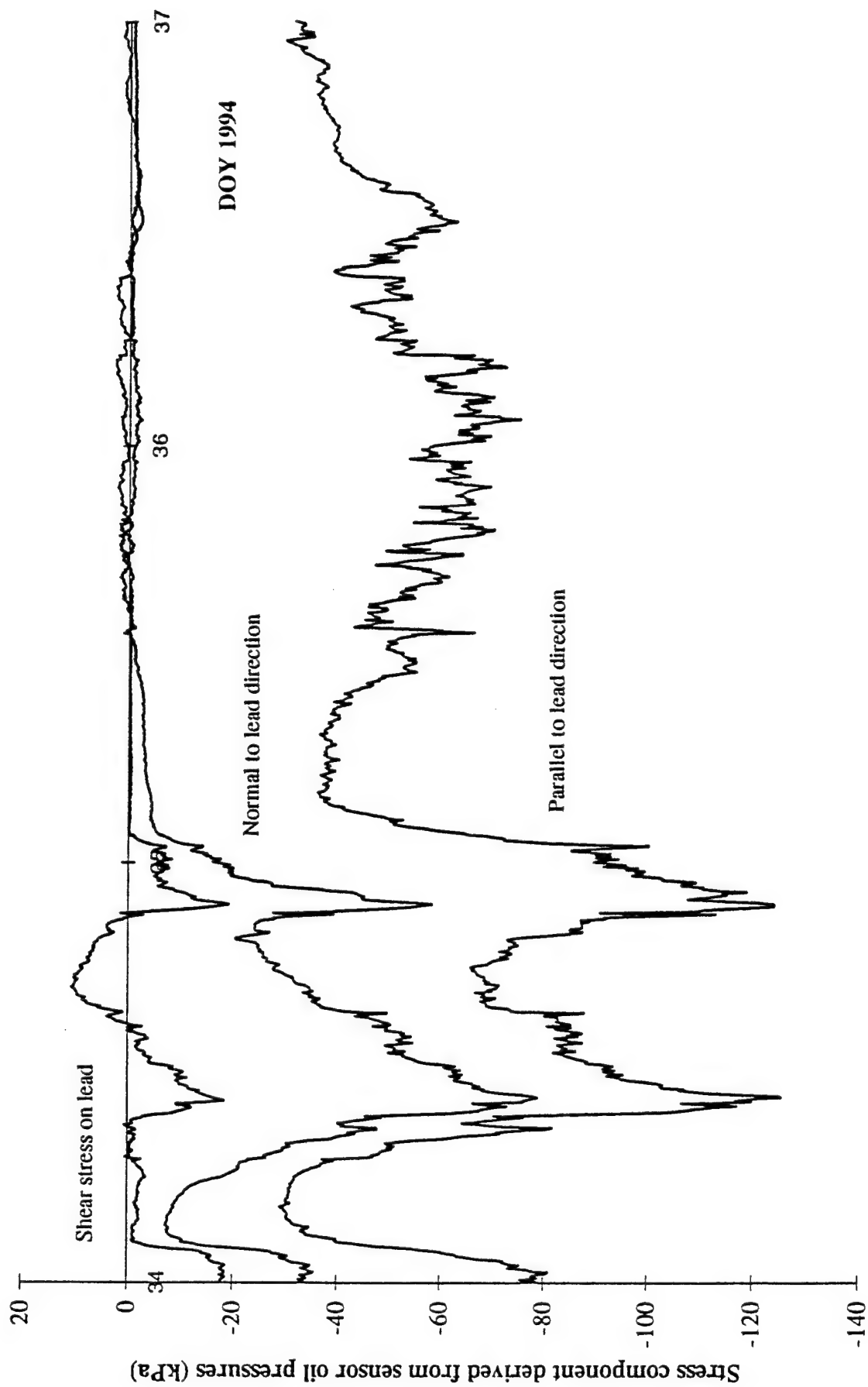
Figure 7. Stress components at Buoy 2 on SIMI Floe 4 expressed in lead coordinates.
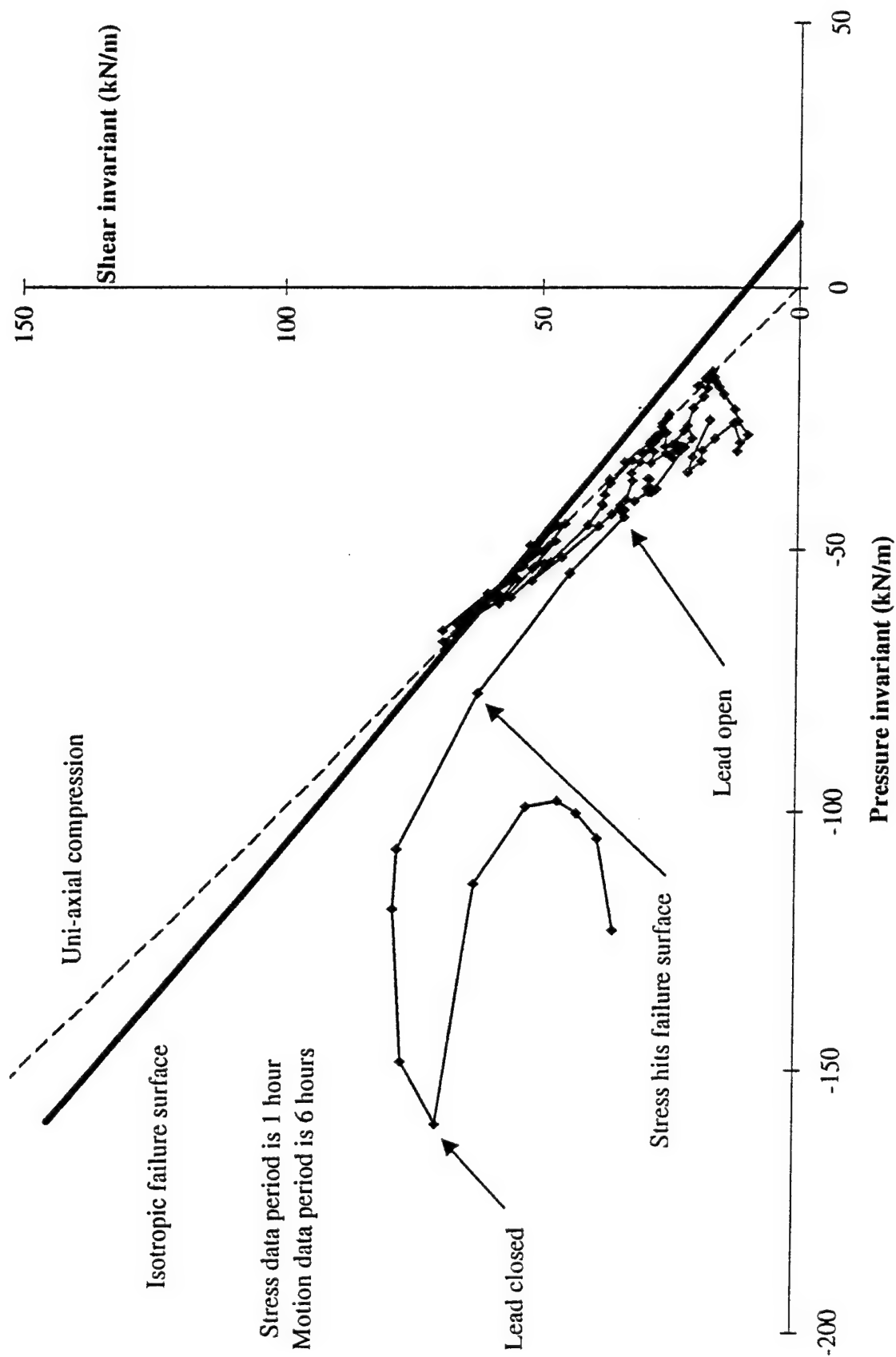
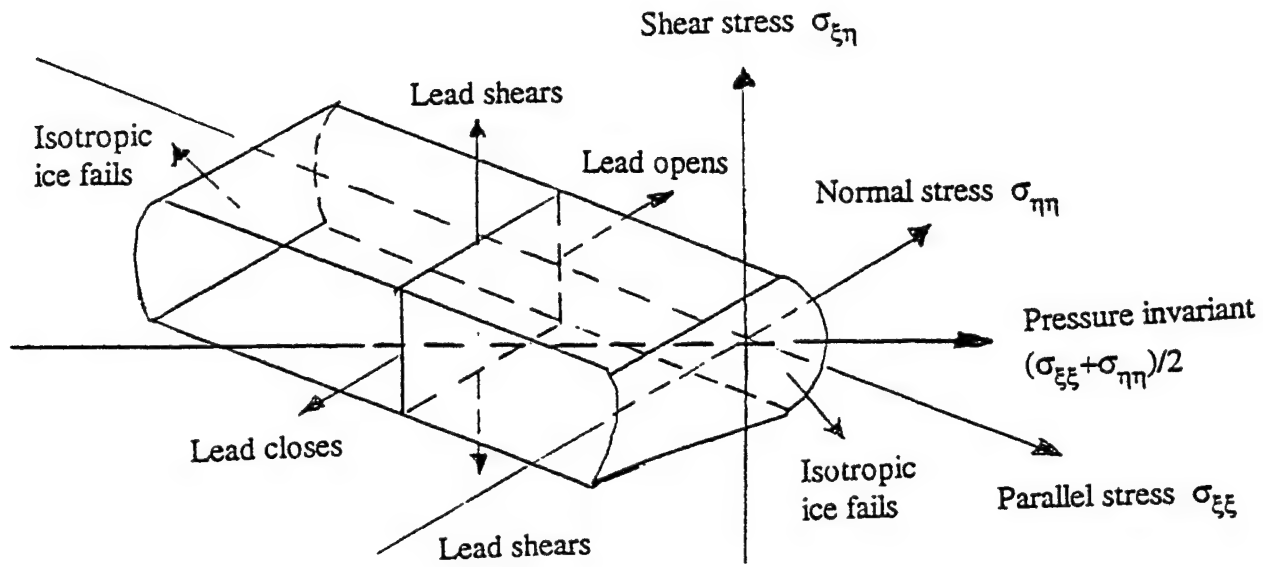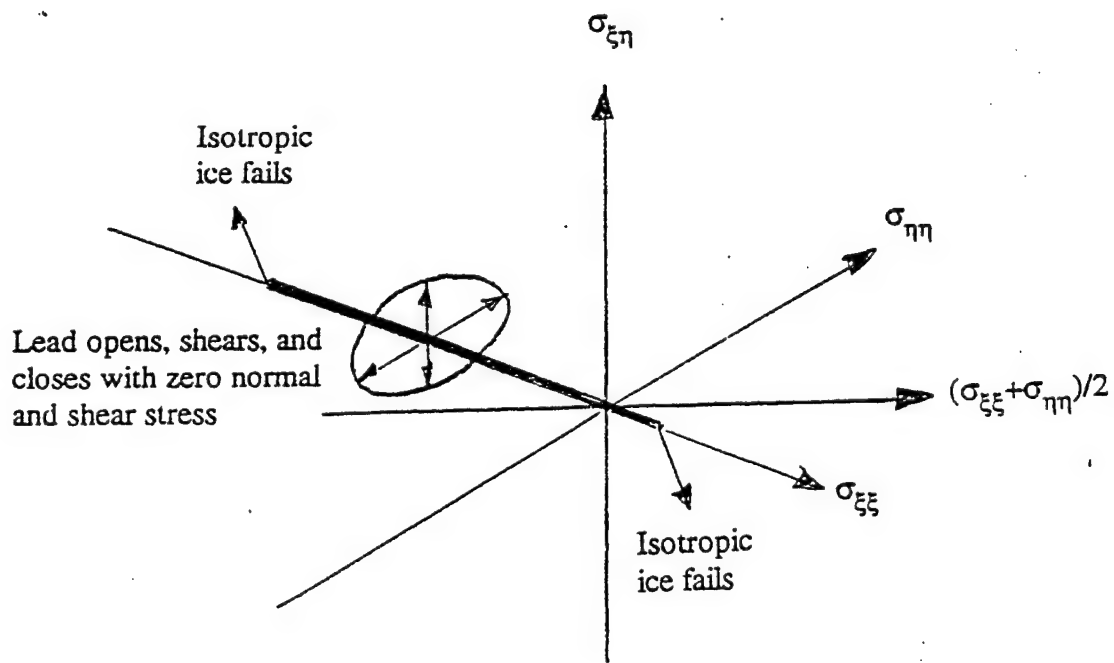**Figure 8.** Stress invariants while lead was active (Days 35-40)
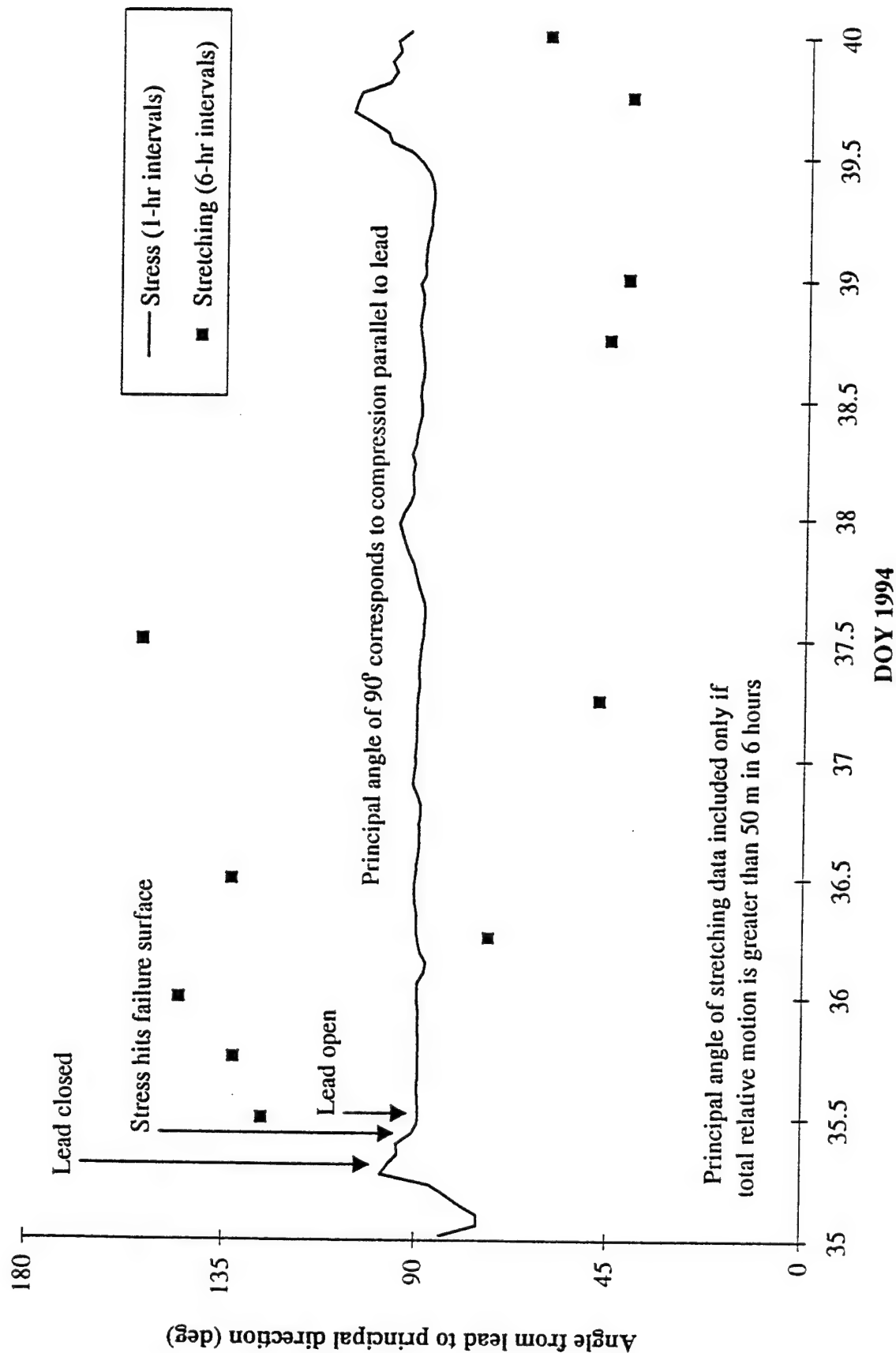
**Figure 9.** Comparison of principal directions for stress and stretching

Shear stress $\sigma_{\xi\eta}$

Lead shears

Isotropic
ice fails

Lead opens

Normal stress $\sigma_{\eta\eta}$

Pressure invariant
$(\sigma_{\xi\xi}+\sigma_{\eta\eta})/2$

Lead closes

Isotropic
ice fails

Parallel stress $\sigma_{\xi\xi}$

Lead shears

(a) Generic lead yield surface

$\sigma_{\xi\eta}$

Isotropic
ice fails

$\sigma_{\eta\eta}$

Lead opens, shears, and
closes with zero normal
and shear stress

$(\sigma_{\xi\xi}+\sigma_{\eta\eta})/2$

$\sigma_{\xi\xi}$

Isotropic
ice fails

(b) Lead yield surface with open water

Figure 10. Oriented ice failure surfaces
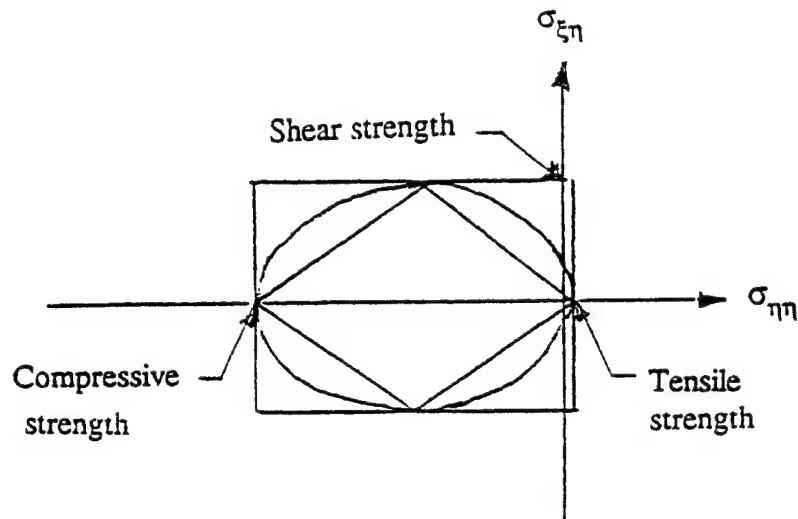
(c) Suitable cross-sections for the lead yield surface may be a rectangle (used here), a diamond, an ellipse, etc.
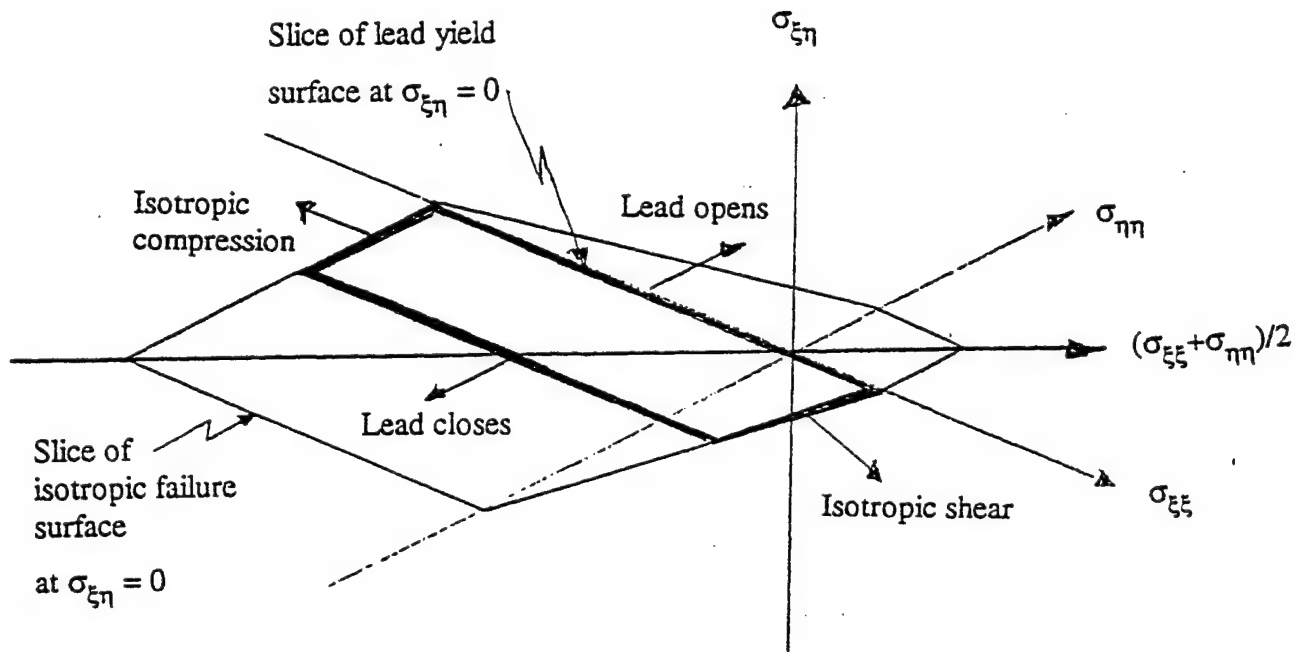


(d) Slice of isotropic failure surface and lead yield surface at zero lead shear stress

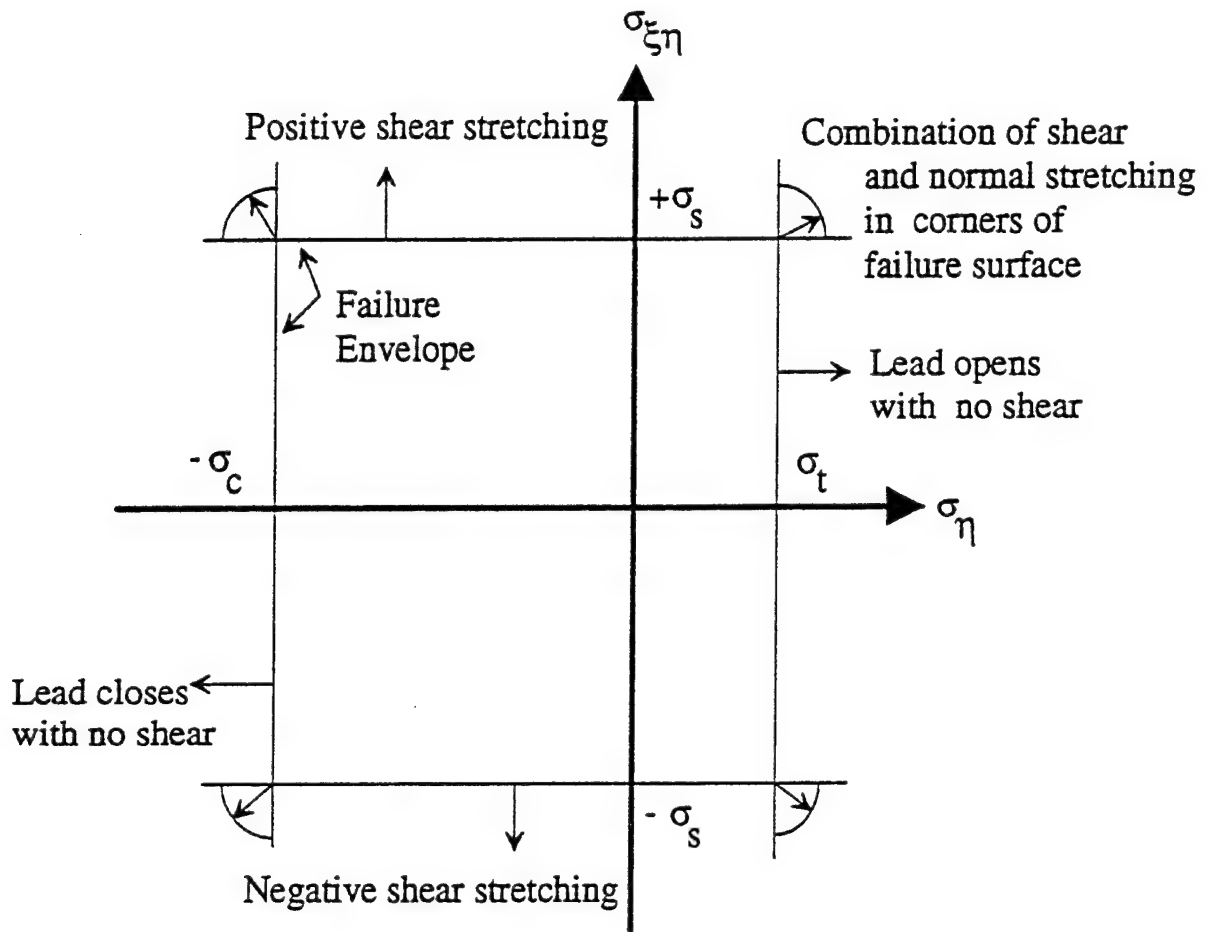**Figure 10.** Oriented ice failure surfaces (continued)

**Figure 11.** *Oriented* ice failure surfaces with associated normal flow rule

# Task 2

# Geophysical Pack-Ice Stress Measurements

# Geophysical pack-ice stress measurements

Max D. Coon, Gerald S. Knoke, and Douglas C. Echert
NorthWest Research Associates, Inc.
Bellevue, WA, USA

## ABSTRACT

This paper describes the determination of geophysical pack-ice stress from sea-ice stress measurements made during the U.S. Navy Office of Naval Research Sea Ice Mechanics Initiative field program and describes the interpretation of the data in terms of a pack-ice failure surface. This effort involved two steps: learning how to interpret sensor oil pressure as ice stress, and learning under what conditions the measured ice stress represents the geophysical stress. These data are shown consistent with the indentation pressure-area curve, which represents the strength of ice over scales from laboratory samples to pack ice elements of hundreds of kilometers.

## INTRODUCTION

This paper reports on the measurement of sea ice stress for many months during the U.S. Navy's Office of Naval Research (ONR) Sea Ice Mechanics Initiative (SIMI) field program during the winter of 1993-1994. The autumn-1994 segment of the SIMI field program is described in Coon et al. (1994). Coon et al. (1989) describe the stress sensors and the installation of the sensors in rosettes to measure the stress state in the ice. We attempted to not only measure ice stress but also geophysical pack-ice stress resultant. The distinction is that the former is a local measurement (which varies with position within a floe) and the latter is an integral through the ice thickness and an average over a few kilometers. Geophysical ice stress resultants are needed in large-scale ice-dynamics models.

## JUSTIFICATION FOR INTERPRETING THIS DATA AS LARGE-SCALE STRESS

It has been suggested that it is not possible to measure geophysical pack-ice stress resultant by making a few stress measurements in one floe. We present data showing that stress measurements represent the sum of local stresses and geophysical stresses and that geophysical stress can be determined. Our goals were that (1) the oil pressure in the stress sensor could be interpreted in terms of ice stress and (2) the local stresses could be calculated and subtracted from the measured stress to acquire the geophysical stress. Three examples are shown to support the hypothesis that the sensor oil pressures can be related to geophysical ice stress.

The first example was a ridge-building event observed by the scientists and crew aboard the Norwegian research ship *Polarbjörn* on October 7, 1988 (Coon et al., 1989). At the time, a sea-ice stress rosette was installed about 300 meters away. The stress data show that the direction of the largest compressive principal stress points in the direction perpendicular to the ridge when it is building. Prior to the riding event, the principal directions had large variations as shown in the data from Coon et al. (1989).

The second example is the stress and deformation of a lead at its creation reported by Coon et al. (1995b). Simultaneous measurements of sea ice stress on both sides of a lead, ice motion from sequential SAR imagery, and ice motion from drifting GPS/Argos buoys are

04/30/97

compared. The lead, which appeared early in Day 35 (Feb. 4), 1994, was observed, relative motions were calculated across and along the lead direction, and stresses were transformed to this same coordinate system. The lead orientation and approximate location were determined from SAR images of the pack ice surrounding the SIMI camp, as well as net ice motion at 3-day intervals. The ice motion around the lead was provided in greater temporal detail by an array of drifting GPS/Argos buoys producing hourly positions. Sea-ice stress was measured on each side of the lead using flat-jack sensors.

Since the calculation of sea-ice stress from sensor oil pressure will affect all sensors in a rosette equally, we calculated "stress" components directly from the sensor oil pressures and the orientation of the sensors. Figure 1 shows these "stress" components in lead coordinates. Shortly before a lead-opening motion is apparent in the ice motion data, the ice-stress state abruptly changed from bi-axial compression to uni-axial compression, with traction on the lead near zero. The stress path in stress invariant space is shown in Figure 2. The principal stress direction turned until it was nearly parallel to the new lead and remained that way for over a week. The principal stress normal to the lead dropped to zero just before the lead opened and the stress remained that way for over a week. The principal stress parallel to the lead was variable but remained large.

The third example is related to determining the failure surfaces for pack ice. Stress analyses in Croasdale et al. (1986) indicated that the stresses in the central portion of the floe reflect the average stress on the floe perimeter with a reasonable degree of accuracy for a wide range of loading conditions. Hence, Croasdale et al. suggested deploying stress rosettes near the center of a large ice floe in the pack ice. In essence, a large floe may be used as a transducer for measuring large-scale pack ice driving forces. Coon et al. (1995a) report sea-ice stresses measured in numerous locations in "Lake Andy," a large area of flat, thin ice contained within the very uneven, 3-km floe with the SIMI main camp in the fall of 1993. Even as late as March 1994, Lake Andy was still over a kilometer from the edge of the floe. NWRA installed eight stress sensors in Lake Andy for a winter-over experiment. All of the stress sensors were far from the "shore," being many characteristics lengths for edge bending effects from shore (Hetenyi, 1946). These sensors should have been exposed to the same ice stress conditions, whether they were geophysical or thermal stresses. Figure 3 (not to scale) shows the relative orientation of these stress sensors. Various combinations were used to form stress rosettes of various sizes ranging from 3 to 100 meters. All of these sensors were installed at 35 cm except stress sensor e, which was taken to be the average of sensors at 20 cm and 50 cm. Stress sensors c, e, f, and g are all the same orientation. Along with stress sensors a and b, these four sensors formed four rosette combinations with diameters of 3, 10, 50, and 100 meters. Again, we calculated "stress" components directly from the sensor oil pressures and the orientation of the sensors; these "stress" components are combined to form the first and second stress invariants, the pressure and shear invariants. A calibration factor affects all sensors equally and, therefore, appears as a scaling factor on both invariants. Thermal stress affects only the pressure invariant but should affect all sensors equally as well. Figures 4-7 show the resulting four stress-invariant charts, using stress invariants calculated directly from three-hour averages of the sensor oil pressures. Although there is some variation among the four combinations, these four rosettes have essentially the same stress envelopes, making the data useful for pack-ice modeling.

## SEA-ICE STRESS DATA PROCESSING PROCEDURE

NWRA has developed a sea-ice-stress data-processing procedure that combines numerous features. For the SIMI data, we have stress data at one depth, temperature data at multiple depths, ice thickness sampled at a few times, salinity at one time, and in-situ calibration test data on many sensors but not all. The sea ice data processing procedure developed by NWRA is summarized below.

1. Process in-situ calibration test data on the stress sensors taken at several load rates.
2. Interpolate the ice thickness data.
3. Calculate the distribution of the elastic modulus, E, through the thickness using the ice temperature, salinity, and interpolated ice thickness data.
4. Remove the slow changes in stress sensor oil pressure resulting from the freeze-in stresses, and the sensor pressurization cycles.
5. Remove the long-term trends from ice temperature data to account for creep in thermal stress.
6. Compare the de-trended stress sensor oil pressure and the de-trended temperature data at the sensor depth and remove sensor temperature effects, if any.
7. Process the resulting stress sensor oil pressure to produce ice stress based on the time-dependent model developed from the in-situ calibration tests.
8. Calculate the thermal stress at stress sensor depth using the de-trended temperature data at all depths and adjust the magnitude of these thermal stress histories to fit the measured stress during pure thermal events.
9. Subtract the calculated thermal stress from the ice stress.
10. Subtract the stress at the depth of the stress sensor due to the bending moment caused by the large-scale stress and the variation in the elastic modulus with depth, if any.
11. Keep only the data when at least three sensors in a rosette have oil pressure over 20 kPa for the entire creep-integration period.

The appendix provides details on the application of this procedure to the SIMI stress data.

## FAILURE SURFACE FOR LARGE-SCALE STRESS

Based on the events and data discussed above, we conclude that sea-ice stress measurements represent large-scale pack-ice stress averaged over the dimension of the typical floe used to measure the pack-ice stress, 1 to 3 km. The strength parameters defining a failure surface using this stress data also represent averages over 1 to 3 km.

The outer envelope of the ice-stress data actually provides an upper bound for the pack-ice failure surface because the pack ice strength is often smaller than the outer envelope due to the presence of thin ice. This envelope represents the failure surface for *isotropic* pack ice as defined by Coon et al. (1992 and 1997).

Figure 8 shows the SIMI ice stress data (0.7-m to 1.6-m ice) with no correction for thermal stress. The data shown on the figure are hourly averages for only those hours that have three or four sensors reading over 20-kPa oil pressure for the entire hour. This was done because our calibration tests and other analyses showed these sensors to be an unreliable method to measure tension and low compressive stresses.

Figure 9 shows the same SIMI data but with the correction for thermal stress. Since the shear invariant is unaffected by the thermal stresses, the individual data points have moved

04/30/97

horizontally as compared to Figure 8. It is worthwhile to note that the measurements were made in a wide range of ice thickness: 0.7 to 1.6 m. These results appear to be independent of the ice sheet thickness in which the sensors were installed.

After inspection of this sea-ice-stress data, we concluded that the isotropic failure surface of the pack ice is best characterized by a Coulomb failure surface. It is represented by three lines on the pressure-invariant plot: in-plane-shear failure, out-of-plane compressive failure, and out-of-plane tensile failure. The Coulomb failure mechanism is well characterized in the literature for soils (e.g., Bowles, 1968), for sea ice at the laboratory scale (e.g., Coon et al., 1984), and for pack ice (e.g., Pritchard, 1988).

Figure 9 also shows lines indicating the recommended Coulomb failure surface. The recommended failure surface is isotropic in three dimensions and has only an unconfined compressive strength $\sigma_c$ and an unconfined tensile strength $\sigma_t$. The corresponding strength parameters are a compressive strength of 250 kN/m and a tensile strength of 50 kN/m. These strengths are consistent with those used in large-scale ice dynamics models. Pritchard (1993) concludes from models of observed events that the unconfined compressive strength must exceed 150 kN/m and the shear strength must exceed 27 kN/m.

Corresponding values for the Coulomb cohesion C and the friction angle $\phi$ for the recommended Coulomb failure surface are 56 kN/m and 42°, respectively. The steeper slope on the right represents out-of-plane tensile failure; the more gently sloped line on the right represents in-plane shear failure; and the sloped line on the left represents out-of-plane compressive failure. The out-of-plane compressive strength is the same as the in-plane compressive strength. This failure surface represents the maximum pack-ice strength at a scale of 1 to 3 km. It is applicable to an ice dynamics model only if the anisotropic effects of leads are incorporated into the model. This failure surface is also applicable to determining ice loads on a structure where it is imperative to know the maximum strength of ice on this scale.

## COMPARISON TO OTHER DATA

Figure 10 compares the recommended Coulomb failure surface to the largest yield surfaces used by Pritchard (1980) and Hibler (1980) in isotropic ice-dynamics models. The isotropic failure surfaces shown in the figure correspond to compact, heavy ice conditions and have a maximum strength of 100 kN/m. Under less compact ice conditions with more thin ice, Pritchard and Hibler use much smaller isotropic failure surfaces, as discussed by Sanderson (1988). Their isotropic strengths were chosen such that the velocity field in model runs would "best" represent the measured velocity field in some average sense. It appears that the measured stress data does not fit inside the large-scale isotropic yield surface very well.

The meaning of "large scale" is, however, very important here and can best be examined by looking at the strength of ice over many scales. To this end, NWRA has developed a procedure to use sea-ice stress data to add data points to the pressure-area curve for ice indentation (Sanderson, 1988). Figure 9 showed all of our SIMI sea-ice stress data plotted as stress-resultant invariants, where the stress resultant is the integral of the measured ice stress though the ice thickness at the stress measurement site. These ice stress data were all measured near the center of ice floes that were 1 to 3 meters thick and 1 to 3 km across. As discussed above, these ice stress data represent the average stress around the perimeter of the instrumented floe and the data shows a maximum compressive strength of 250 kN/m.

04/30/97

To compare this data to the pressure-area curve, we consider the instrumented floe to be a large indentor. Coon et al. (1984) discuss the relationship between indentation pressure and material properties such as compressive strength and friction angle. Equation (17) in Coon et al. (1984) shows that indentation pressure equals the compressive strength for very large values of the indentor (floe) diameter to ice thickness aspect ratio. Since the aspect ratio in this case is very large, the indentation factor is one. Consequently, the maximum indentation pressure is simply the maximum compressive strength.

These SIMI stress data can now be plotted on Sanderson's pressure-area curve. For the stated ranges in ice thickness, indentor diameter, and maximum compressive strength, the indentation pressures range from 0.08 to 0.25 MPa and the contact areas range from 1000 to 9000 m$^2$. Figure 11 shows the excellent agreement. Sanderson has derived indentation pressures from the isotropic yield surfaces used by Pritchard (1980) and Hibler (1980). These are shown as "Meso-scale models" in the lower right corner of Figure 10 for maximum strengths ranging from 5 to 100 kN/m.

As a general rule, for scales from 0.1 cm to 500 km, sea ice strength and indentation pressure are controlled by three sea ice rheologies with three constitutive laws:

1.  For laboratory scale and intact sea ice (indentor width from 0.1 cm to 10 m), mechanical properties (e.g., elastic modulus, compressive strength) are known to depend upon grain size, brine volume, temperature, and strain rates. Indentation pressure depends upon mechanical properties, indentor aspect ratio, and the specific failure mechanism (e.g., in plane or out-of-plane, Tresca or Coulomb).

2.  An ice floe is a jointed material, like igneous rock. For an indentor width from 100 to 500 m, the compressive strength is controlled by the cohesion, friction, and spacing of the joints (brine-filled cracks) occurring every 100 to 300 m in first-year and multi-year sea ice. The intact ice between joints does not participate since the joints are perhaps 100 times weaker than the intact ice.

3.  Pack ice at the geophysical scale (1 to 500 km), deformations occur along leads and ridges spaced at 10 to 50 km; the ice floes do not participate. Buckling, rafting, and ridging failure mechanisms (which depend upon the refrozen lead ice thickness) control the compressive strength and cause anisotropy in the pack-ice strength.

## CONCLUSIONS

The SIMI stress data show that it is possible to measure geophysical pack-ice stress. In addition, we conclude that it is inappropriate to scale down large-scale isotropic ice behavior to a cell size of a few kilometers without separately modeling the (anisotropic) leads and ridges.

## APPENDIX A. PROCEDURE FOR SEA-ICE STRESS DATA PROCESSING

### Calibration tests

NWRA used thin, circular, oil-filled flat-jack ice stress sensors to measure sea ice stress during ONR's SIMI Program (Coon et al., 1995a; Coon et al., 1995b). To calibrate these sensors, we performed in-situ compression tests at two speeds: rapid loading (around 100 kPa/min.), which produced a square-wave pressure history, and slow loading (around one

04/30/97

kPa/min.), which produced a ramp pressure history. The load rate of the ramp tests more closely matched geophysical load rates, while the rapid load rate of the square-wave test is fast enough to measure the elastic response of the ice-sensor system. A large, flat air jack was used to compress the ice containing the stress sensor. The calibration tests were run at separate sensor installations except for one rosette that was tested after a 1-meter crack made the site unusable. Based on the properties of sea ice (see Michel, 1978, for example) and the test results, we chose to model the response of the sensor to ice stress with a dynamic inclusion factor of the form

$$\sigma = -AP - \int_{t-\tau_0}^{t} BPd\tau \tag{1}$$

where $\sigma$ is the ice stress normal to the sensor or the air pressure in the air jack, P is the oil pressure in the sensor, and A, B, and $\tau_0$ are constants.

By plotting the air pressure versus the oil pressure found in the square-wave tests, we obtained the effective elastic-inclusion factor, A, for the sensor installed first-year sea ice. In many of these plots, a change in slope occurs at 10 to 20 kPa oil pressure. We judged that the stress sensor readings are unreliable whenever the oil pressure is less than 20 kPa and, therefore, concluded that these sensors do not measure tensile stresses or small compressive stresses. The creep terms in the dynamic inclusion factor, B and $\tau_0$, were determined using the linear up-ramp portion of each ramp test along with the effective elastic inclusion factor from a prior square-wave test at the same installation. The measured air pressure for the whole test was compared with the air pressure calculated from the oil pressure and the model.

Although many such square-wave and ramp tests were performed, eight tests were selected as valid determining generic values for A, B, and $\tau_0$. Invalid ramp tests were rejected for any one of the following reasons:

- The oil pressure never reached 20 kPa,
- The linear ramp time after the oil reached 20 kPa was too short (e.g., less than 40 minutes),
- The oil pressure data was polluted by external ice stress (e.g. thermal and geophysical stresses).

We found no correlation of tests results to any of the following parameters:

- The sensor diameter (15 or 20 cm),
- Time of year (fall or spring in first-year ice),
- Air jack stand-off distance (15 or 30 cm or both on opposite sides),
- The measured elastic modulus of the stress sensor.

The creep model accounts for the effects of the air-jack-loading rate. Although we could model an individual test well, the standard deviation of A, B, and $\tau_0$ for the eight valid tests were 37%, 57%, and 64% of there values, respectively. We have chosen to use the following values:

$$A = 2.43 \qquad B = -0.037 \text{ min.}^{-1} \qquad \tau_0 = 20 \text{ min.} \tag{2}$$

Using these mean values, the standard deviation of the calculated value of the maximum air pressure during the eight ramp tests is 64 kPa.

04/30/97

**Converting SIMI ice stress measurements to geophysical stress resultants**

The NWRA SIMI stress rosettes consisted of four sensors installed at 45° compass intervals and at roughly mid-depth near the middle of a large expanse of flat, first-year sea ice. Three rosettes were installed in the autumn in roughly 70-cm ice; one was moved in the spring to a fourth site in 1.6-meter flat, first-year ice. Time and oil-pressure data was stored on site by dataloggers onto storage modules at 5-minute intervals and a 10-minute-interval data set was transmitted to the Argos satellite system. Consequently, the data interval is five minutes for the initial portion of each data stream from all four sites but is ten minutes for the final portion for the three rosettes that were lost at sea.

To assure contact between the sensor and the creeping sea ice, all sensors were pressurized at regular intervals by adding oil to the sensor until the pressure increased by at least 70 kPa. A minimum of two hours of data was lost for the pressurization cycle. After pressurization, the added pressure creeps out, rapidly at first, then slower. We modeled this process as the sum of fast and slow exponential decays, fit each pressurization cycle for each sensor, and subtracted the double-exponential curve from the oil pressure. The two exponential time constants were approximately three hours and 14 days. The remaining oil pressure was processed with the dynamic inclusion-factor model to generate ice stress. Whenever the remaining oil pressure was less than 20 kPa, the data was dropped because of our findings in the square-wave calibration tests mentioned above. Because Equation (2) requires 20 minutes of data, the first 20 minutes after any data dropout is lost as well.

The ice stress measured by the sensor is our best estimate of the ice stress at the depth of the sensor in the ice sheet, but we seek the geophysical ice stress resultant. For that, we need to account for ice thickness, elastic modulus variations through the ice thickness, thermal stress, and bending stress. The ice thickness determined from drilling holes and from thermistors installed with the stress rosette was consistent at the first three sites; growth in ice thickness was interpolated in proportion to the square root of time. Cox and Weeks (1988) give estimates for the distribution of the elastic modulus through the ice thickness for various thicknesses of first-year sheet ice. We approximated their results with a constant elastic modulus for the top 80% of thickness and zero for the bottom 20%. With this distribution, there is no correction needed for bending stress as long as the sensor is in the top 80% of the ice sheet.

A theory for the stresses due to temperature gradients in an unconfined, thick, elastic plate of uniform thickness in which the temperatures and the properties are a function only of depth is given by Timoshenko and Goodier (1951):

$$\sigma_{xx} = \sigma_{yy} = -\frac{\alpha E \Delta T}{1-\nu} + \frac{1}{h(1-\nu)} \int_{-h/2}^{h/2} \alpha E \Delta T dz - \frac{12y}{h^3(1-\nu)} \int_{-h/2}^{h/2} \alpha E \Delta T z dz \qquad (3)$$

where x and y are the coordinates in the plane of the plate, z is the coordinate down from the mid-depth of the plate, $\sigma$ is the stress at z, $\alpha$ is the thermal expansion coefficient, E is the elastic modulus, $\Delta T$ is the temperature change from a uniform temperature as a function of z, $\nu$ is the Poisson's ratio for the material, and h is the plate thickness. The depth used to evaluate the first term on the right side of Equation (3) is the depth of the resulting stresses on the left side. For the ice sheet, we need to evaluate the thermal stress at the depth of the sensor, $\alpha$ is essentially constant, and E is zero for the bottom 20% of the depth. The thermal stress is sea ice is thus

04/30/97

$$\sigma_{xx} = \sigma_{yy} = \frac{\alpha E}{1-\nu}\left\{-\Delta T + \frac{1}{h}\int_{-0.3h}^{0.5h}\Delta T dz - \frac{12y}{h^3}\int_{-0.3h}^{0.5h}\Delta T z dz\right\} \tag{4}$$

The ice temperatures were measured with thermistors at several depths. To account for the creep out of the thermal stress, we calculated the temperature change not from an initial uniform temperature but from a reference temperature calculated by smoothing the measured temperatures with a low-pass filter. The filter has a 14-day time constant, which is the same time constant as the slow creep found in the pressurization decay. Constant values of 1 GPa for the effective elastic modulus, 0.3 for Poisson's ratio, and $5.1 \times 10^{-5}$ per °C for the thermal expansion coefficient were found to make the calculated thermal stress, which is the same in all (horizontal) directions, consistent with the ice stress measured with all four sensors in the rosettes. These values are similar to those used by Lewis (1993) in his calculations of thermal stress in sea ice. Lewis, however, uses a variable elastic modulus, a different definition for a reference temperature, and creep strain in his model.

The geophysical stress resultant is the integral of the geophysical stress through the thickness of the ice sheet. Since the elastic modulus is constant for the top 80% of the thickness, the difference of the ice stress and the thermal stress is the geophysical stress for that layer. The bottom 20% must have no stress since the elastic modulus is zero, so the geophysical stress resultant is 0.8h times the difference of ice and thermal stress.

In order to calculate the geophysical stress-resultant invariants, at least three sensors in a rosette need to have valid data for 20 minutes. When that was true, we calculated the invariants by one of the following two sets of equations. When sensors a, b, and c were valid, Equations (5) and (6) provide the invariants:

$$\sigma_I = \frac{1}{2}\left(\sigma_a + \sigma_c\right) \tag{5}$$

$$\sigma_{II} = \sqrt{\frac{1}{2}\left(\sigma_a - \sigma_b\right)^2 + \frac{1}{2}\left(\sigma_b - \sigma_c\right)^2} \tag{6}$$

where $\sigma_a$, $\sigma_b$, and $\sigma_c$ represent the geophysical stress resultant derived from three sensors spaced at 45° intervals. Similar equations are used for the other sets of three, as appropriate; the substitutions in the equation follow the rule that sensors a and c must be at right angles to each other. When all four sensors are valid, the invariants that best fit the four sensors readings are given by

$$\sigma_I = \frac{1}{4}\left(\sigma_a + \sigma_b + \sigma_c + \sigma_d\right) \tag{7}$$

$$\sigma_{II} = \frac{1}{2}\sqrt{\left(\sigma_a - \sigma_c\right)^2 + \left(\sigma_b - \sigma_d\right)^2} \tag{8}$$

where $\sigma_a$, $\sigma_b$, $\sigma_c$, and $\sigma_d$ represent the geophysical stress resultant derived from four sensors spaced at 45° intervals.

## ACKNOWLEDGMENTS

## REFERENCES

Bowles, J. E., *Foundation Analysis and Design*, McGraw-Hill Book Company, New York, NY, 1968.

Coon, M. D., A review of AIDJEX modeling, in *Sea Ice Processes and Models*, edited by R. S. Pritchard, pp. 12-27, University of Washington Press, Seattle, 1980.

Coon, M. D., R. J. Evans, and D. H. Gibson, Failure criteria for sea ice and loads resulting from crushing, in *Proceedings of International Association for Hydraulic Research Ice Symposium 1984*, Vol. III, Hamburg, 1984.

Coon and Associates, Failure criteria for sea ice and loads resulting from crushing, Alaska Oil and Gas Association Project #260 Final Report, 1985.

Coon, M. D., P. A. Lau, S. H. Bailey, and B. J. Taylor, Observations of ice floe stress in the eastern Arctic, *POAC '89, The 10th International Conference on Port and Ocean Engineering under Arctic Conditions*, Volume 1, Proceedings, Luleå, Sweden, 1989.

Coon, M. D., D. C. Echert, and G. S. Knoke, Pack ice anisotropic constitutive model, *IAHR 92 Proceedings of the 11th International Symposium on Ice*, Banff, Alberta, pp. 1188-1205, 1992.

Coon, M. D., G. S. Knoke, D. C. Echert, and H. L. Stern, Contemporaneous field measurements of pack ice stress and ice strain measurements from SAR imagery, in *Proceedings of OCEANS'93*, Victoria, B. C., October, 1993.

Coon, M. D., G. S. Knoke, and D. C. Echert, The Sea Ice Mechanics Initiative (SIMI), in *Proceedings of the 26th Annual OTC Conference*, Houston, TX, May, 1994.

Coon, M. D., D. C. Echert, G. S. Knoke, J. E. Overland, S. Salo, R. S. Pritchard, D. A. Rothrock, and H. L. Stern, Sea ice deformation and stress, a comparison across space scales," in *Proceedings of the Sea Ice Mechanics and Arctic Modeling Workshop*, Anchorage, AK, April 25-28, Vol. 2, 1995a.

Coon, M. D., D. C. Echert, and G. S. Knoke, Sea ice mechanics research, in *Proceedings of the Sea Ice Mechanics and Arctic Modeling Workshop*, Anchorage, AK, April 25-28, 1995, Vol. 1, pp. 151-159, 1995b.

Coon, M. D., G. S. Knoke, D. C. Echert, and R. S. Pritchard, An oriented thickness distribution for sea ice, submitted to *Journal of Geophysical Research*, April 1997.

Cox, G. F. N., and W. F. Weeks, Numerical simulations of the profile properties of undeformed first-year sea ice during the growth season, *Journal of Geophysical Research*, Vol. 93, No. C10, pp. 12,449-12,460, 1988.

Croasdale, K. R., G. Comfort, and B. W. Graham, Arctic Pack-Ice Forces Research Project, 1986," Report to Government of Canada, Dept. of Fisheries and Oceans, Institute for Ocean Sciences, Sidney, BC, Canada, 1986.

Dempsey, J. P., Scale effects on the splitting strength of sea ice," NEB96 Ice Load Workshop, Calgary, Alberta, March 13-15, 1996.

04/30/97

Golombek, M. P. and W. B. Banerdt, Constraints on the subsurface structure of Europa," *Icarus*, Vol. 83, pp. 441-452, 1990.

Hamza, H. and D. Blanchet, A study of the creep effect upon the response of a pressure sensor embedded in an ice sheet," *Cold Regions Science and Technology*, Vol. 9, pp. 97-107, 1984.

Hetenyi, M., *Beams on an Elastic Foundation*, The University of Michigan Press, Ann Arbor, MI, 1946.

Hibler, W. D., Modeling pack ice as a viscous-plastic continuum: some preliminary results, in *Sea Ice Processes and Models*, ed. R. S. Pritchard, University of Washington Press, pp. 163-176, 1980.

Lewis, J. K., A model for thermally-induced stresses in multi-year sea ice, *Cold Regions Science and Technology*, Vol. 21, pp. 337-348, 1993.

Michel, B., *Ice Mechanics*, Les Presses de l'Université Laval, Québec, Canada, 1978.

Overland, J. E., B. A. Walter, T. B. Curtin, and P. Turet, Hierarchy and sea ice mechanics: A case study from the Beaufort Sea, *Journal of Geophysical Research*, Vol. 100, No. C3, pp. 4,559-4,571, March 15, 1995.

Pritchard, R. S., Mathematical characteristics of sea ice dynamics models, *Journal of Geophysical Research*, Vol. 93, No. C12, pp. 15,609-618, 1988.

Pritchard, R. S., A simulation of nearshore winder ice dynamics in the Beaufort Sea, in *Sea Ice Processes and Models*, ed. R. S. Pritchard, University of Washington Press, pp. 49-61, 1980.

Pritchard, R. S., Sea ice constitutive behavior and under-ice noise," *Natural Physical Sources of Underwater Sound: Sea Surface Sound (2)*," edited by B. R. Kerman, Kluwer Academic Publishers, Boston, MA, pp. 591-610, 1993.

Sanderson, T. J. O., *Ice Mechanics, Risks to Offshore Structures*, Graham and Trotman, Inc., Kluwer Academic Publishers Group, Norwell, MA, 1988.

Templeton, J. S. III, Measurement of sea ice pressures, in *POAC 79, The Fifth International Conference on Port and Ocean Engineering under Arctic Conditions*, Trondheim, Norway, August 13-18, Proceedings Volume 1, pp. 73-87, 1979.

Templeton, J. S. III, Analysis for an embedded ice pressure sensor, *Transaction of the ASME, Journal of Energy Resources Technology*, Vol. 103, pp. 87-95, 1981.

Timoshenko, S., and J. N. Goodier, *Theory of Elasticity*, McGraw-Hill, New York, NY, 1951.

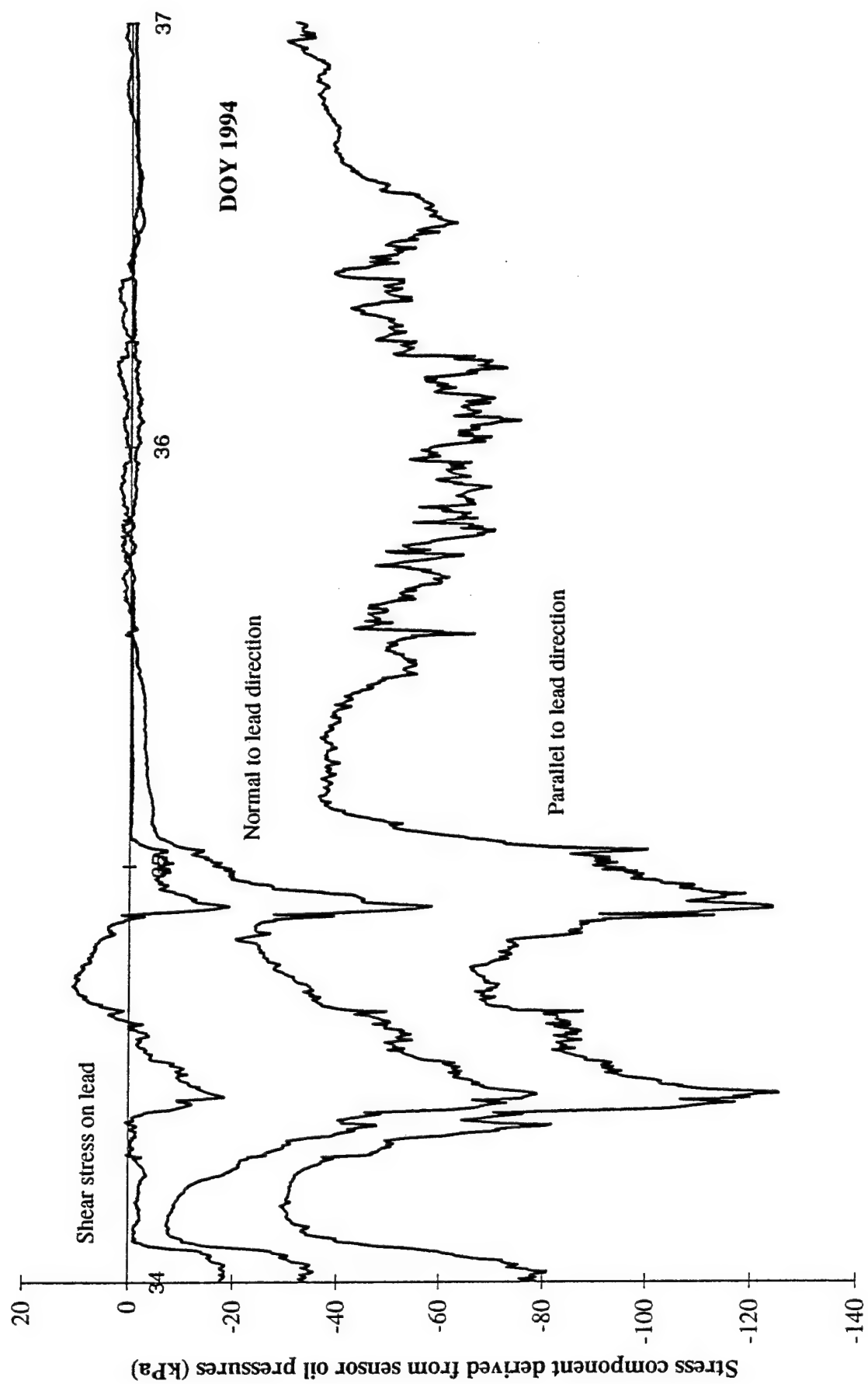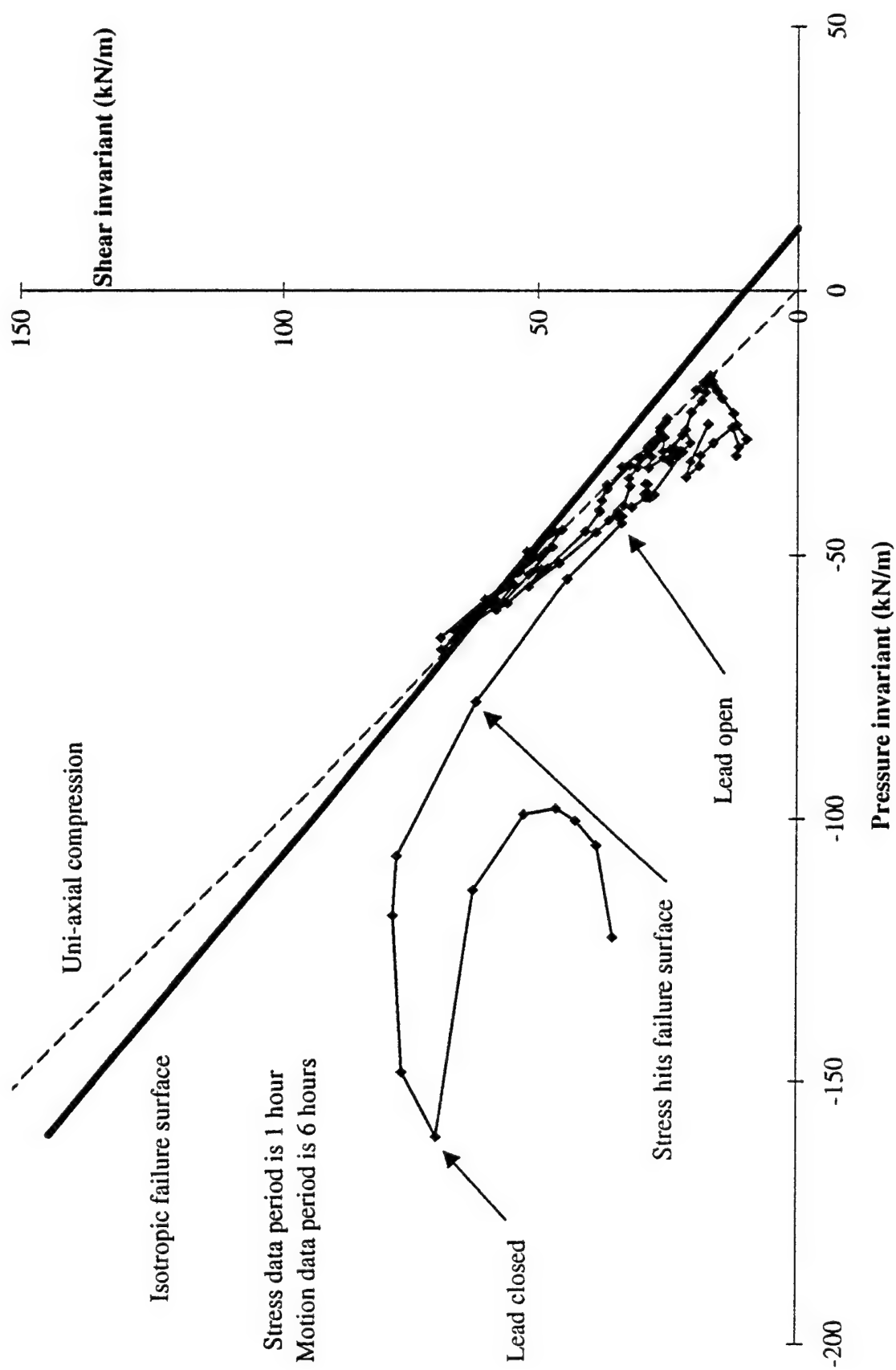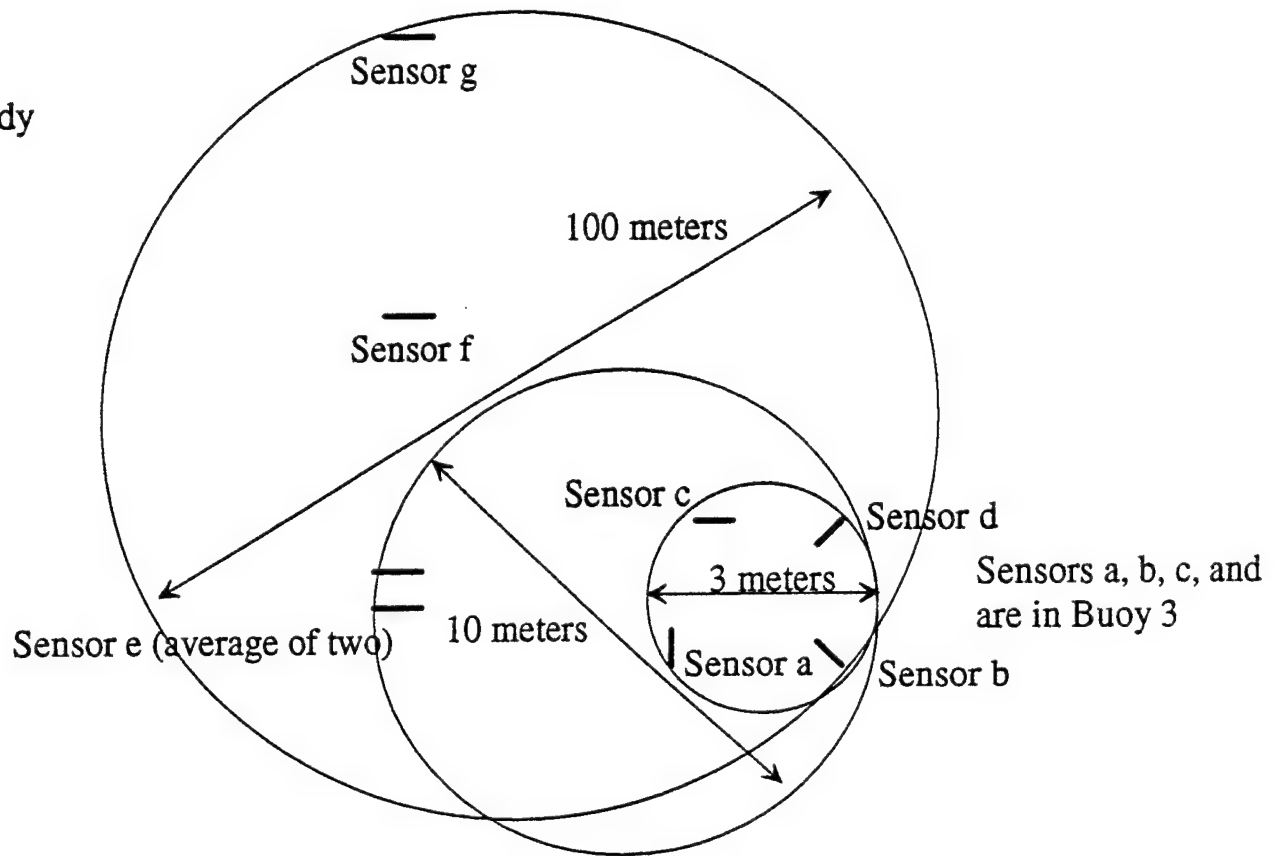## LIST OF FIGURES

04/30/97

04/30/97

Figure 1. Stress components at Buoy 2 on SIMI Floe 4 expressed in lead coordinates.

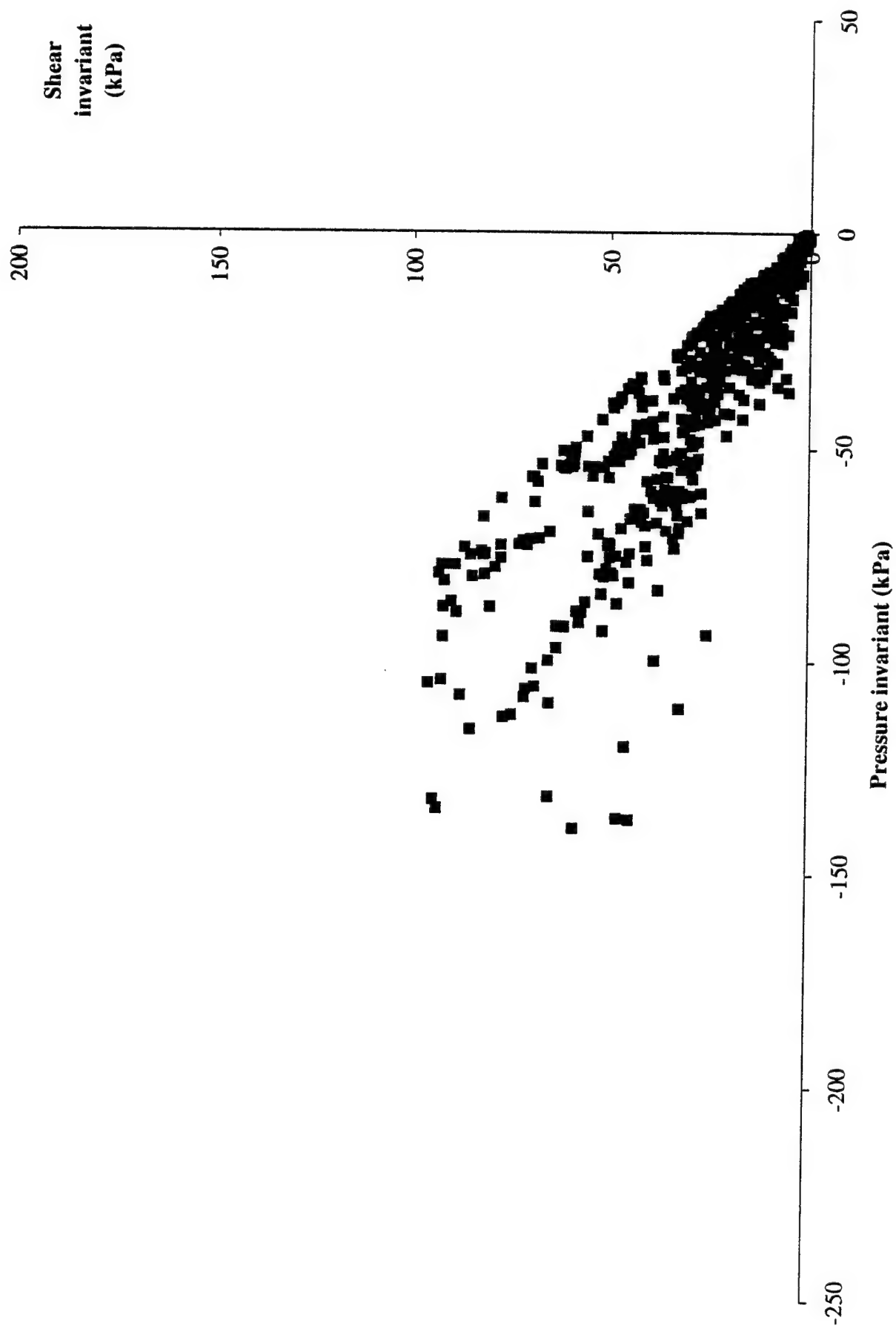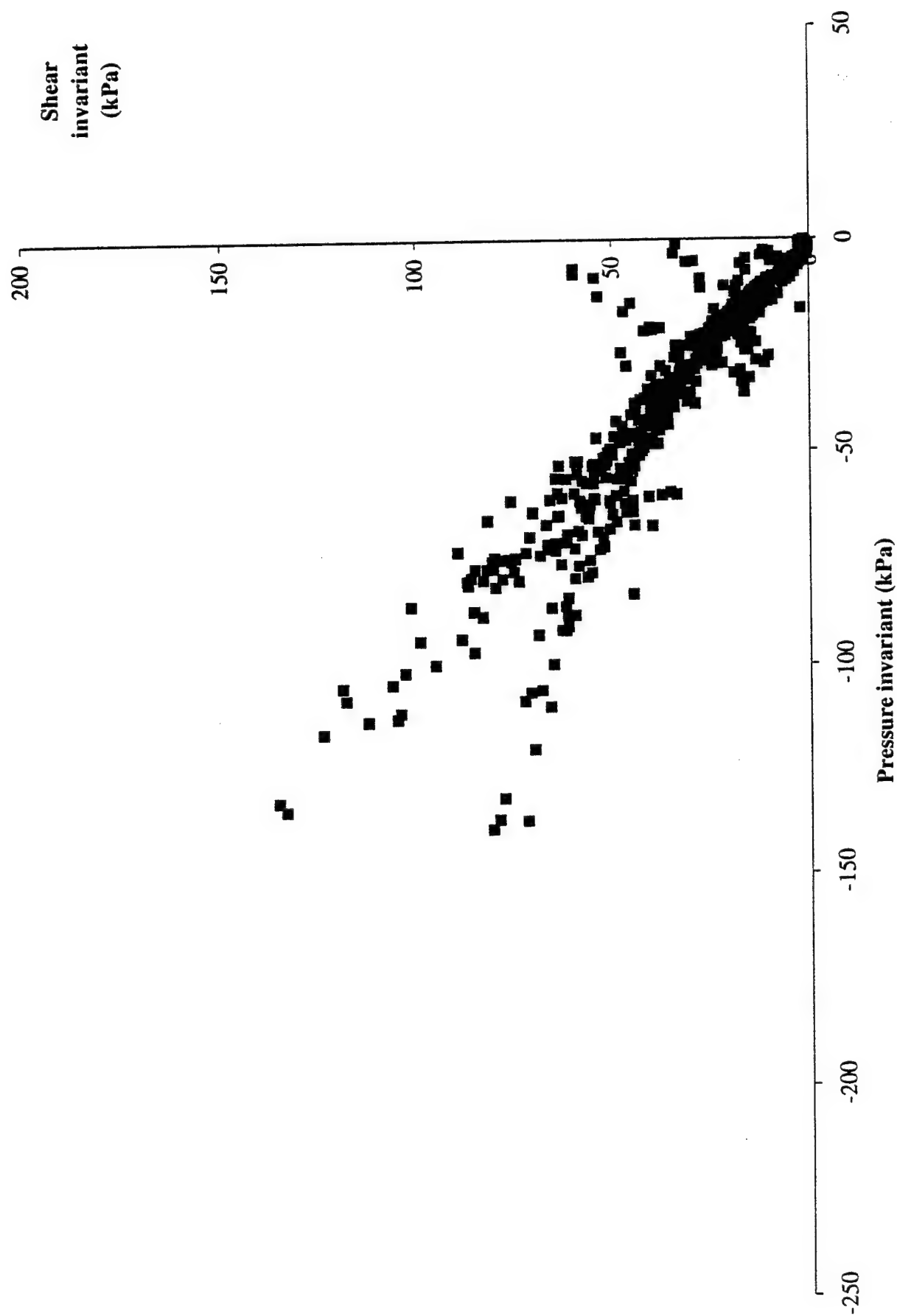**Figure 2.** Stress invariants while lead was active (Days 35-40)

**Figure 3.** Relative orientation of Buoy 3 and other stress sensors in Lake Andy near SIMI camp
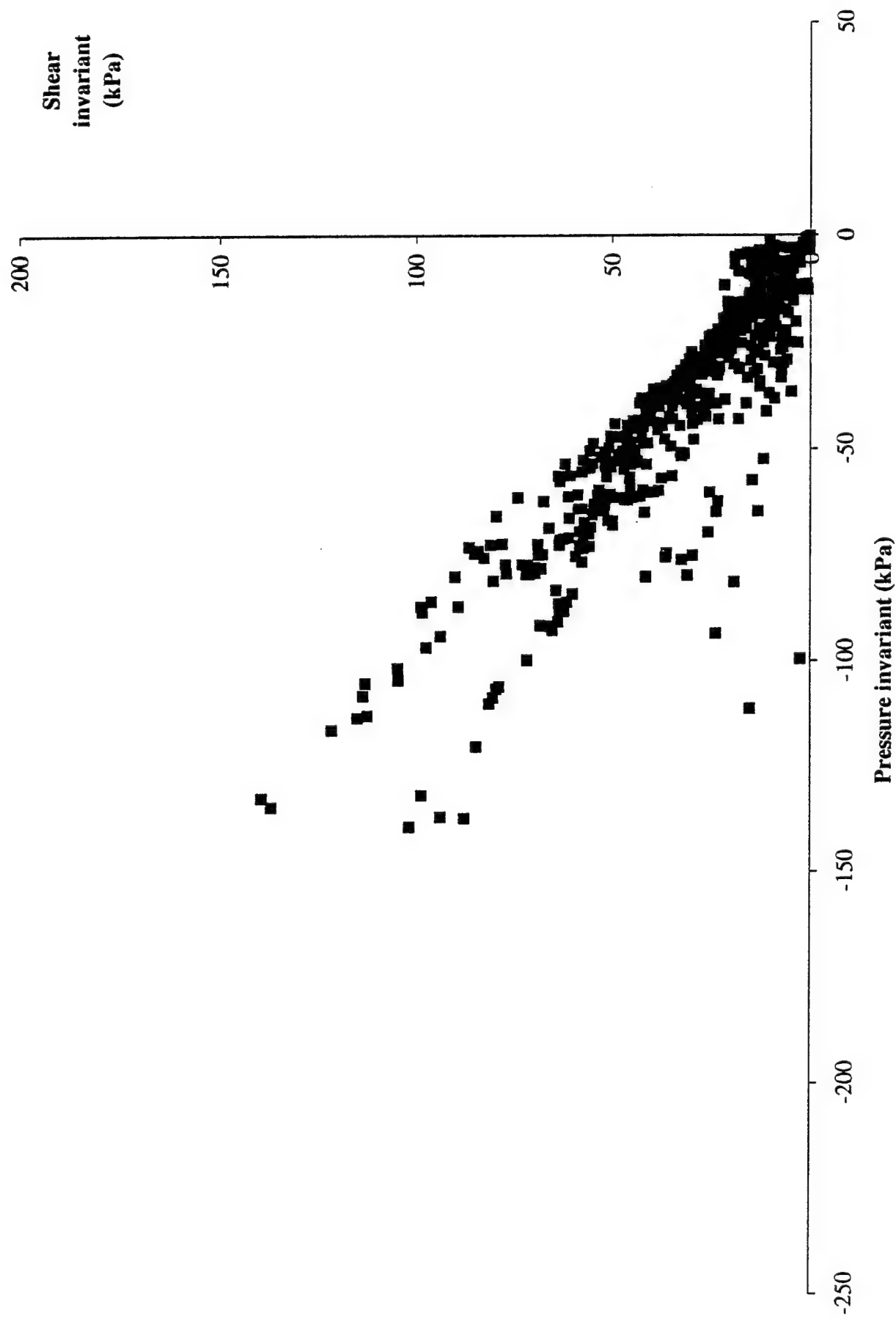
**Figure 4.** Stress invariants from Buoy 3 (sensors b, c, and d) (three-hour averages for December 1993 to February 1994).

**Figure 5.** Stress invariants from Buoy 3 (sensors b and d) and Lake Andy site (sensor e) (three-hour averages for December 1993 to February 1994).
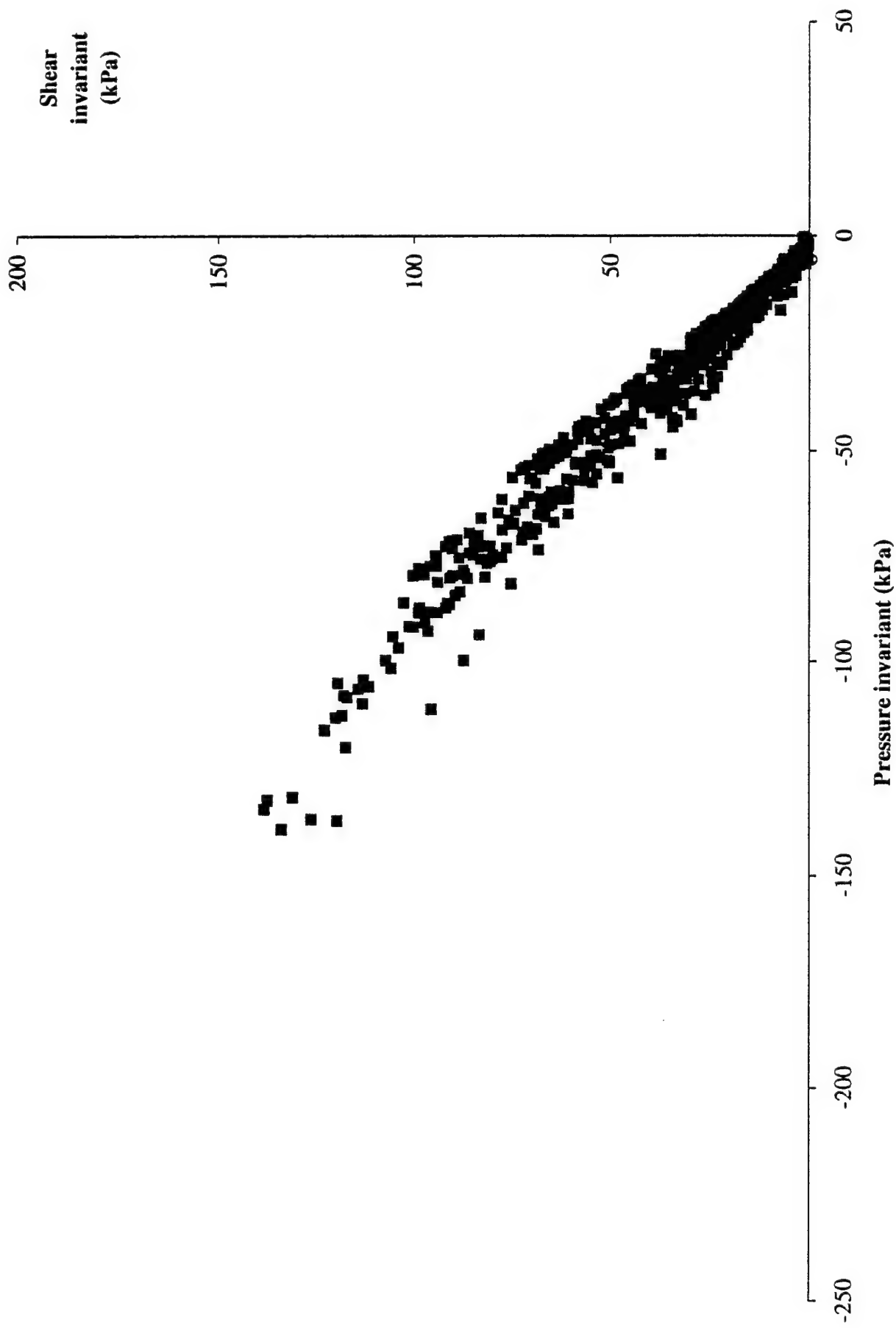
**Figure 6.** Stress invariants from Buoy 3 (sensors b and d) and Lake Andy site (sensor f) (three-hour averages for December 1993 to February 1994).

**Figure 7.** Stress invariants from Buoy 3 (sensors b and d) and Lake Andy site (sensor g) (three-hour averages for December 1993 to February 1994).
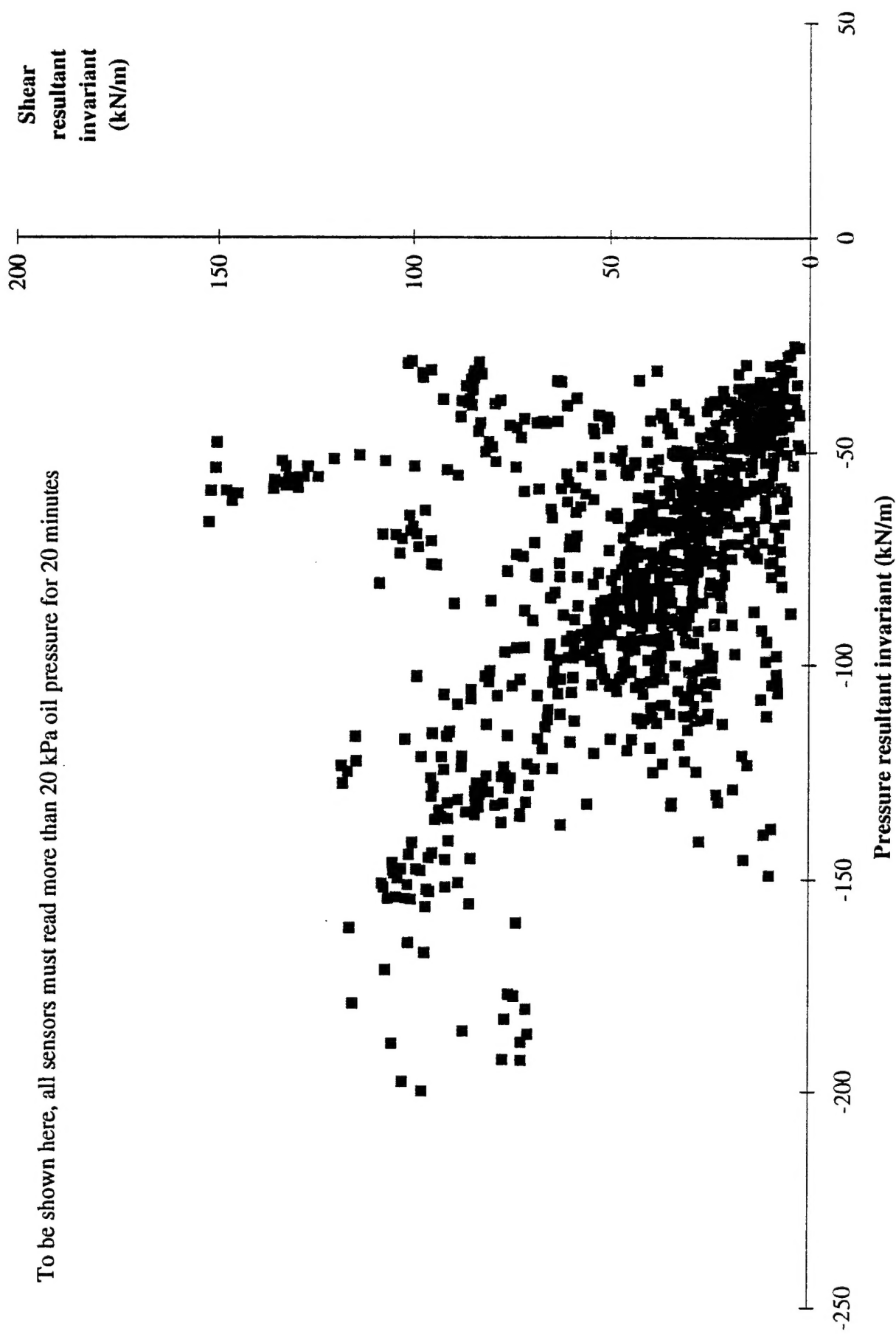
**Figure 8.** SIMI stress-resultant invariants (hourly averages, no thermal stress correction)
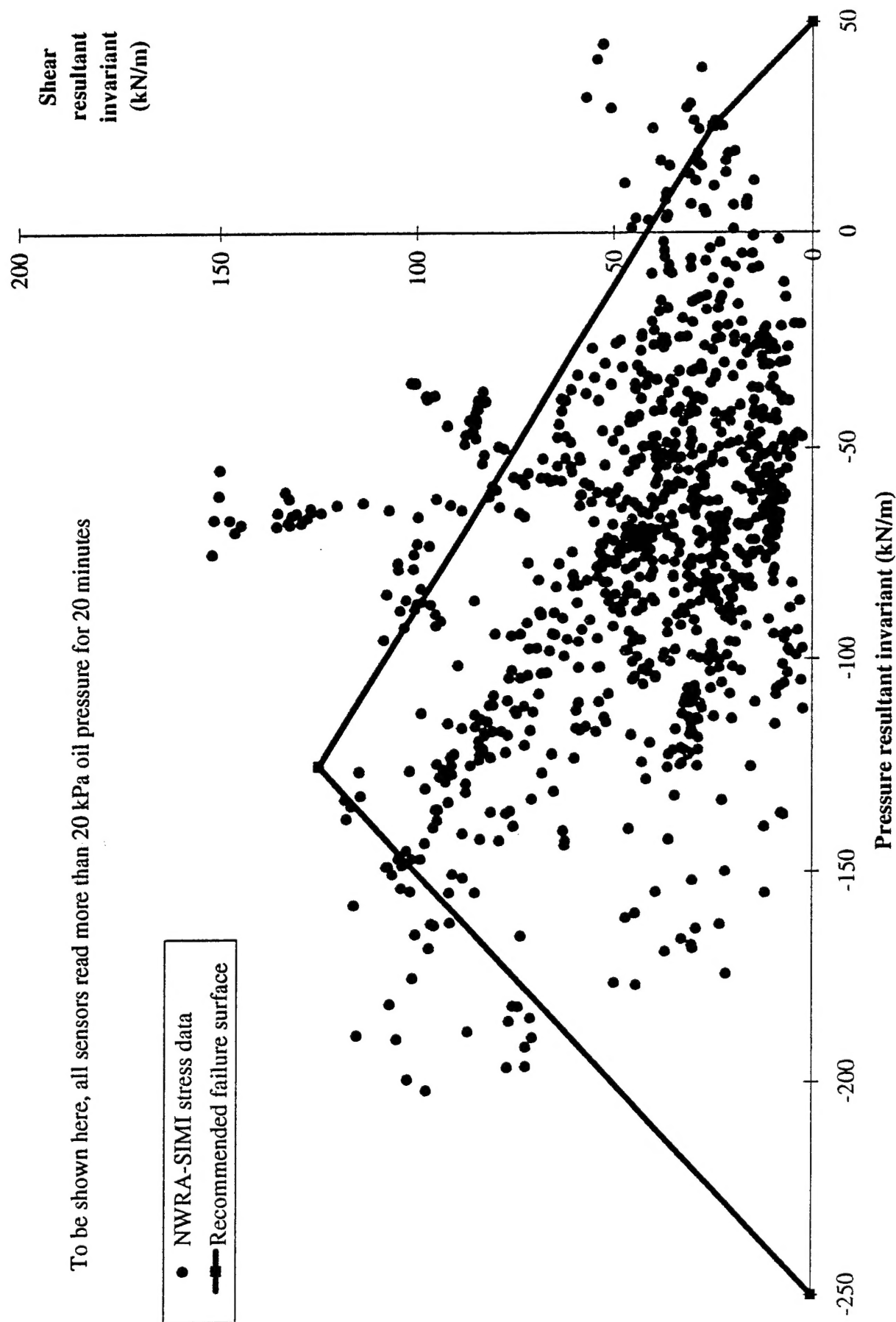
To be shown here, all sensors read more than 20 kPa oil pressure for 20 minutes

Shear resultant invariant (kN/m)

- NWRA-SIMI stress data
- Recommended failure surface

Pressure resultant invariant (kN/m)

**Figure 9.** Stress-resultant invariants (hourly averages with thermal correction) and recommended failure surface
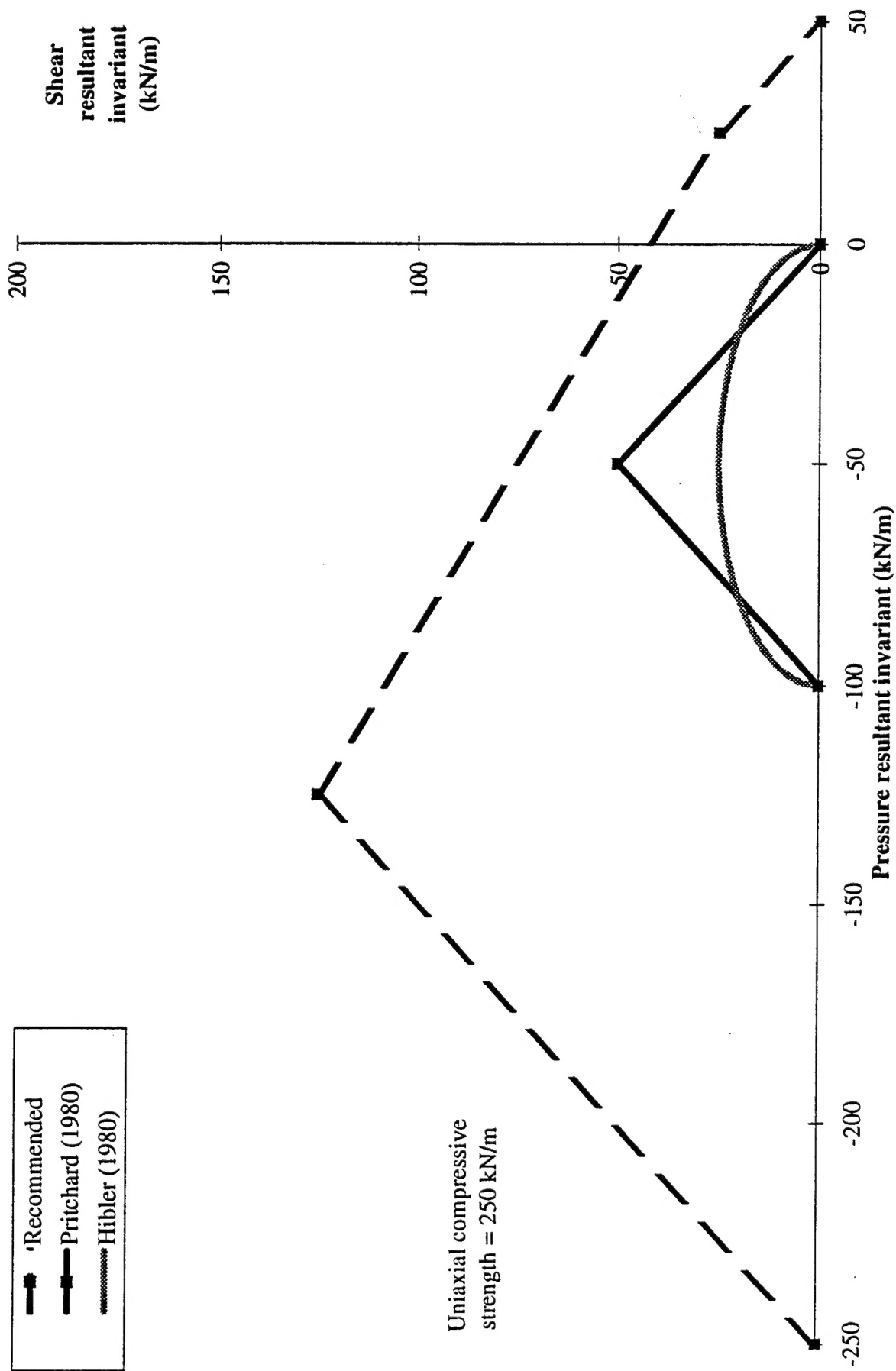
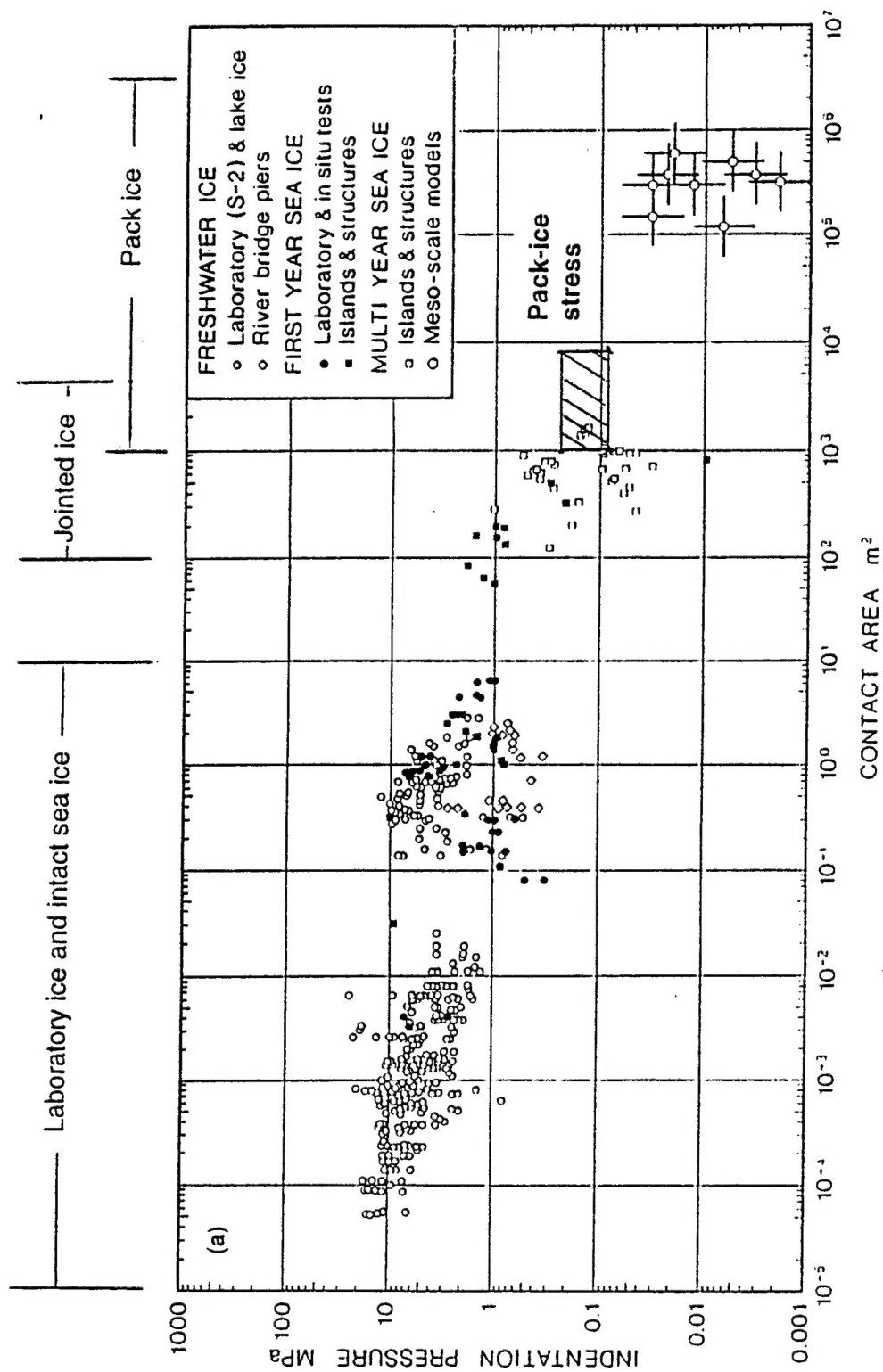**Figure 10.** Comparison of recommended failure surface to past isotropic failure surfaces used in ice-dynamics models.

**Figure 11.** Indentation pressure-area curve with SIMI stress data.